



# LUND UNIVERSITY

## Fire-induced radiological integrated assessment

### aerosol characterization

Malmborg, Vilhelm; Pagels, Joakim; Gudmundsson, Anders; Gren, Louise; Madsen, Dan; van Hees, Patrick; Barton, John

2019

#### Document Version:

Publisher's PDF, also known as Version of record

[Link to publication](#)

#### Citation for published version (APA):

Malmborg, V., Pagels, J., Gudmundsson, A., Gren, L., Madsen, D., van Hees, P., & Barton, J. (2019). *Fire-induced radiological integrated assessment: aerosol characterization*. Lund University.

#### Total number of authors:

7

#### Creative Commons License:

Unspecified

#### General rights

Unless other specific re-use rights are stated the following general rights apply:

Copyright and moral rights for the publications made accessible in the public portal are retained by the authors and/or other copyright owners and it is a condition of accessing publications that users recognise and abide by the legal requirements associated with these rights.

- Users may download and print one copy of any publication from the public portal for the purpose of private study or research.
- You may not further distribute the material or use it for any profit-making activity or commercial gain
- You may freely distribute the URL identifying the publication in the public portal

Read more about Creative commons licenses: <https://creativecommons.org/licenses/>

#### Take down policy

If you believe that this document breaches copyright please contact us providing details, and we will remove access to the work immediately and investigate your claim.

LUND UNIVERSITY

PO Box 117  
221 00 Lund  
+46 46-222 00 00

# **Fire-Induced Radiological Integrated Assessment**

## **— Aerosol Characterization**

WP-AT: T-LU-AD\_FD-01 Soot Testing Campaign: Deliverable AD-01 and AD-02

Date: 30th of June 2019

*Vilhelm Malmborg, Louise Gren, Anders Gudmundsson and Joakim Pagels*  
*Division of Ergonomics & Aerosol Technology,*  
*Faculty of Engineering, Lund University*

&

*Dan Madsen, John Barton & Patrick van Hees*  
*Division of Fire Safety Engineering, Faculty of Engineering, Lund University*



**LUND**  
UNIVERSITY



# 1 Summary

This report on detailed aerosol characterization of fire smoke emissions is part of the Fire-Induced Radiological Integrated Assessment (FIRIA; CERN, Switzerland). In this study, carried out at Lund University, a number of materials were combusted in a cone calorimeter at varied heat fluxes. In a few experiments, the effect of reduced O<sub>2</sub> content of supply air was investigated (vitiating conditions). The materials included electrical components, magnets, plastic components, oil and cables and were selected due to their high probability of experiencing ionizing radiation in the research facilities at CERN. The aerosol particle yield in the combustion emissions was determined in terms of number and mass emissions. In addition, the particle physical properties in terms of size distributions, the mass - mobility relationship, and the black carbon fraction of emitted particles was determined. Finally, the particle morphology was determined with transmission electron microscopy (TEM) and elemental composition of trace elements by ICP-MS.

The total range of aerosol mass yields spanned from approximately 0.005 (g/g fuel) to 0.23 (g/g fuel). Electrical components and magnets were identified as the combustibles with highest mass yields. Mass yields for cables spanned from 0.005-0.09 g/g fuel. The emissions were highly dynamic, with rapid shifts in concentrations and the particle number size distribution as measured with a fast mobility spectrometer (DMS500). The number yields ranged from approximately  $0.05 \cdot 10^{14}$  to  $2 \cdot 10^{14}$  emitted particles per gram of fuel and was measured within the size range 5-1000 nm. The emissions could be parameterized for future modelling applications into nucleation mode particles (with geometric mean diameter that varied between 20-50 nm) and accumulation mode particles (with geometric mean diameter 100-230 nm).

The aerosol mass yields were governed primarily by the concentration and size distribution of accumulation mode particles. Mass yields were determined from 1) Impactor measurements (Dekati Gravimetric Impactor) and 2) Simultaneous measurements of the electrical mobility size distribution (DMS500) and effective density distribution (DMA-APM). The general agreement between the two techniques was good ( $R^2=0.93$ ).

Black carbon is indicative of refractory carbonaceous particles which form in fuel rich conditions of the hot flame environment and associated with the black color of soot (smoke). Black carbon yields were for most experiments similar to the derived mass yields. TEM images showed typical refractory black carbon aggregates at high BC fractions. The primary particle size was larger than for diesel exhaust. However, at reduced heat flux and during vitiating combustion (reduced O<sub>2</sub> concentration), black carbon yields were sometimes much lower than the derived particle mass yields. TEM analysis for a sample with low BC fraction showed only very few particles and those that were found had distinctly different properties to the high BC fraction sample. We hypothesize that particles emitted under these conditions were dominated by low volatility organic matter formed in the pyrolysis of the materials. Such components were likely co-emitted with black carbon also in conventional experiments, although in minor mass fractions. Based on previous studies it can be hypothesized that H:C ratios are low for the cases with high BC fraction ( $<0.1$ ), but H:C ratios may be substantially higher for the samples with low BC fraction.

Analysis of larger elements was attempted with ICP-MS. The results show that the yields of such components were substantially lower than for carbonaceous species. However, yields separated by elements require, further more controlled studies.

This new knowledge will be used within FIRIA to carry out improved risk assessments of fire accidents at the large hadron collider (LHC) and other facilities experiencing ionizing radiation at CERN

# Contents

1	Summary .....	3
2	Introduction .....	7
2.1	Fire aerosols and the exposure to particulate matter .....	7
2.2	Aerosol characterization: aim and future implementation .....	7
2.3	Introduction to aerosol science .....	8
3	Experimental methodology .....	10
3.1	Considerations for experimental methodology.....	10
3.2	Aerosol sampling and set-up .....	11
3.2.1	Instrumentation.....	11
3.2.2	Primary aerosol dilution .....	13
3.2.3	Secondary aerosol dilution .....	14
3.3	Derivation of aerosol yield .....	15
3.4	Estimating particle mass from combined DMS500 and APM measurements .....	15
4	Results and discussion.....	17
4.1	Presentation of the primary analysis.....	17
4.1.1	Time-resolved processed test data.....	17
4.1.2	Reduction of the results into a simplified model using bimodal lognormal distribution fitting	19
4.1.3	Effective density distribution .....	21
4.2	Concluding summary of aerosol mass, BC, and particle number yields .....	22
4.2.1	Aerosol yields.....	22
4.2.2	Evaluation of relationships between particle number, mass, and BC yields.....	27
4.2.3	Evaluation of particle mass and effective density .....	29
4.3	Effect of heat flux and vitiated combustion.....	31
4.3.1	Heat flux .....	31
4.3.2	Vitiated combustion .....	32
4.4	Offline analysis on particle morphology and elemental composition .....	34

4.4.1	Particle Imaging by Transmission Electron Microscopy .....	34
4.4.2	Elemental analysis by Inductively Coupled Plasma Mass Spectroscopy .....	36
4.5	Error and sensitivity analysis.....	37
4.5.1	DGI filter weighing .....	37
4.5.2	Sensitivity analysis of the APM and DMS500 mass derivation .....	37
4.5.3	Comparison of aerosol yields derived for the DGI and DMS500 instruments .....	39
5	Conclusions .....	40
6	References .....	41

## 2 Introduction

### 2.1 Fire aerosols and the exposure to particulate matter

Exposure to particles in the air we breathe is associated with far-reaching health effects in the general population. Around 5000 people annually die premature in cardiovascular and pulmonary disease due to exposure to air pollution at the relatively low levels we have in Sweden today (Gustafsson et al. 2014). The corresponding number within Europe is ~400.000. Fine particles (PM<sub>2.5</sub>, particles smaller than 2.5  $\mu\text{m}$ ) is the most important factor. During fires much higher exposures occur, the particles and gases released are also more toxic than those in ambient air. The emissions are distributed over a range of particle sizes and chemical components. When it comes to fires relatively little is known about these parameters and how they relate to material fire properties and combustion conditions.

Hertzberg et al. (2003) showed that particle yields varied between 0.2% and 15% during combustion of a range of materials relevant for fires. They found that the mass median aerodynamic diameter of the released particles was 0.1- 0.4  $\mu\text{m}$ . Only time-integrated data were reported. Perovic (2018) used techniques developed in aerosol technology to follow the number weighted size distribution with high time resolution. The size distribution was commonly bimodal, with a mode of smaller particles (10-50 nm) dominating early and late during the fire, and a mode of larger accumulation mode particles (100-300 nm) dominating during the most intense combustion phase.

When modelling the spread of fire emissions in enclosed volumes, for example during underground work and the eventual spread to ambient air, detailed knowledge about the initial emissions is required. This includes aerosol deposition and coagulation as the plume ages and is diluted with clean air. Particles in fire emissions commonly consist of agglomerated black carbon (soot) particles with complex shapes. This makes modelling of the released plumes more challenging. For example, different equivalent diameters describe deposition and transformation of smaller and larger particles, respectively. Therefore one needs to keep track of both aerodynamic and mobility equivalent diameters during modelling. For other combustion sources such as diesel exhaust there are parameterizations available on the emission levels and size distributions, split up into different size modes (Sakurai et al., 2003) as well as how different equivalent diameters relate to each other and the mass of particles of complex morphology (Park et al., 2003).

### 2.2 Aerosol characterization: aim and future implementation

The aim of this study was to derive detailed information on fire smoke emissions for a range of materials of relevance for the Fire-Induced Radiological Integrated Assessment (FIRIA) conducted at CERN, Switzerland. This included: particle yield in terms of number and mass, particle physical properties in terms of size distributions and mass mobility relationship, and the black carbon (BC) fraction of emitted particles. The aerosol characterization was conducted at the Enoch Thulin Laboratory at Lund University. An experimental methodology enabling the data to be used as input for fire dynamic simulations and aerosol transport models was chosen. This new knowledge will be used by CERN to carry out improved risk assessments of fire accidents at the large hadron collider (LHC) and other facilities experiencing ionizing radiation at CERN.



### 2.3 Introduction to aerosol science

An aerosol is defined as liquid and solid particles suspended in a gas. The particles suspended in the aerosol mixture are small enough to remain airborne for long times. Particle deposition and aerosol dynamics is mainly governed by four mechanisms: gravitational settling, Brownian motion (diffusion), impaction, and electrostatic forces. The downward motion induced by the gravitational force on an aerosol particle is balanced by the friction of air molecules on the particle surface. This results in a terminal settling velocity and an upper size limit to what can be defined as an aerosol particle ( $\sim 100\ \mu\text{m}$ ). Diffusion of aerosol particles, i.e., the random motion induced by collisions with air molecules, depends on the size of particles. Small particles ( $< 0.1\ \mu\text{m}$ ) have high diffusion velocities and large particles ( $> 1\ \mu\text{m}$ ) have very low diffusion velocities. Diffusion also act to alter the aerosol particle size distribution. The high diffusion velocities of small particles makes them susceptible to collisions with other aerosol particles. It can be assumed that upon collision the particles stick together, forming one new aerosol particle. This is called coagulation. Coagulation is an important mechanism in aerosol dynamics as it, with time, reduces the particle number and shifts the particle size distribution to larger sizes. However, mass is conserved.

A third deposition mechanism known as impaction is relevant when the aerosol is set in motion. Impaction occurs when an aerosol flows over an obstacle, forcing the gas molecules to change direction. The inertia of the much larger aerosol particles causes them to continue their initial trajectory for a short distance. This distance is determined by the particle relaxation time which increases with particle size and density. If this distance is long enough the particle can impact on the surface and be deposited. Impaction is a highly relevant mechanism for deposition of particles in human airways. In addition to these mechanisms, a fourth relevant deposition mechanism is the motion induced by electrostatic attraction and repulsion between aerosol particles and surfaces. Electrostatic attraction may also act between aerosol particles and result in enhanced coagulation.

In the atmosphere, the size dependency of these deposition mechanisms causes particles to accumulate for sizes where diffusion, settling and impaction are weak. This occur in a size range between  $\sim 0.1$ - $1\ \mu\text{m}$ , and the particles within these sizes are often termed accumulation mode particles.

The same deposition forces are responsible for the size dependency of particle deposition probabilities in the various parts of the respiratory tract (Figure 1). Diffusion is responsible for the increased deposition of particles below  $0.1\ \mu\text{m}$ . For sizes below  $0.01\ \mu\text{m}$  the diffusivity is so high that a majority of the deposition occurs already in the tracheobronchial and head region. The minimum between  $0.1$  and  $1\ \mu\text{m}$  is clear, in this region most inhaled particles do not deposit and are exhaled. For particles above  $0.5\ \mu\text{m}$ , impaction is the main mechanism for deposition in the head region (nose and throat) and at the bifurcations in the TB region. In the lower respiratory tract, the alveolar region, the main deposition mechanism above  $0.5\ \mu\text{m}$  is sedimentation. Hygroscopic material (for example nitrates and sulphates) takes up water in the humid respiratory tract and particles dominated by such species may increase their diameter by up to a factor of 5. Particles from incomplete combustion are commonly non-hygroscopic.

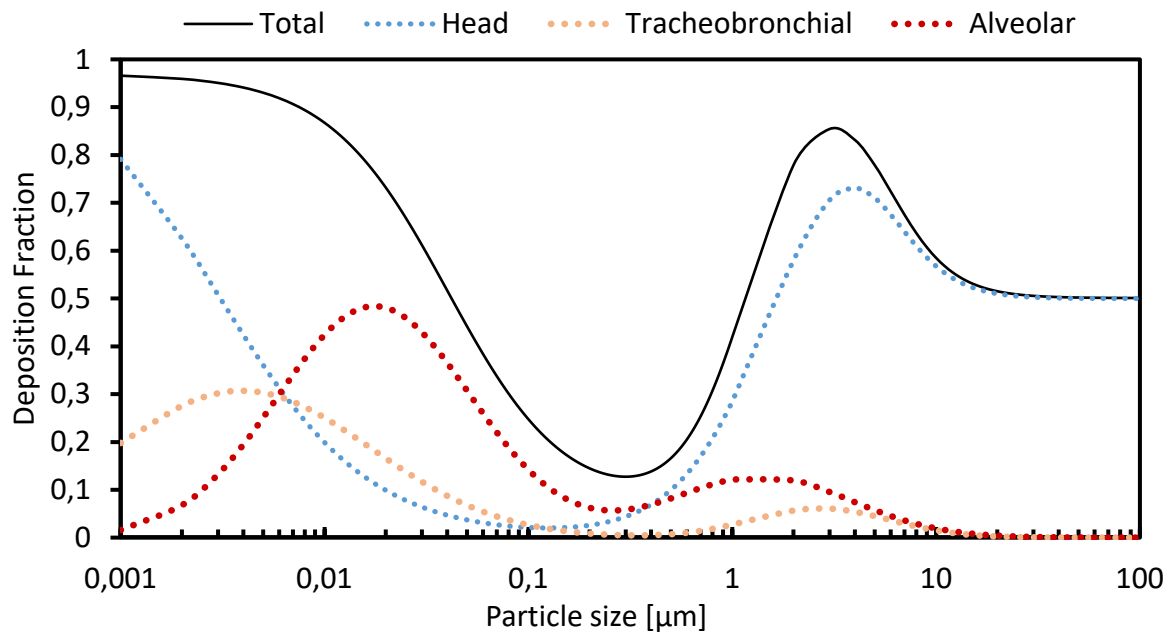


**Figure 1. Deposition probability in the respiratory tract as function of particle size computed for a healthy man at light exercise using the International Commission on Radiological Protection lung deposition model (ICRP, 1994). Courtesy of Malin Alsved & Jonas Jakobsson.**

### 3 Experimental methodology

#### 3.1 Considerations for experimental methodology

From consideration of time and fire condition dependent aerosol formation, aerosol instrumentation with high time resolution were selected as primary means of classification. The DMS500 (Cambustion, Cambridge, UK) (Reavell, 2002; Reavell et al., 2002) and an aethalometer (AE33, Magee Scientific, Berkely, USA) (Drinovec et al., 2015) were selected as primary aerosol instruments. The DMS500 classifies aerosol particles according to number and electrical mobility size (5-1000 nm). The aethalometer classifies aerosol particles according to the equivalent black carbon (BC) mass concentration.

A total of 66 tests were conducted. The DMS500 and aethalometer were included in all tests. In addition, an aerosol particle mass analyzer (APM) was included for more than 30 samples. The APM classifies the particle mass for a given electrical mobility size. From the relationship between particle mobility size and mass the *effective density* can be calculated. Effective density is defined as the density of a perfectly spherical particle of the same mass and electrical mobility as the true particle. Knowledge of the effective density enables derivation of aerosol mass from the combined measurements of DMS500 and APM. The time resolution of the APM is low and the transient conditions of the emissions introduce artefacts in the results. The system was therefore setup to classify the mass of aerosol particles averaged over a time-period of approximately 10 minutes, using a residence time chamber. Knowledge of the particle effective density at a given electrical mobility diameter furthermore allows conversion of the DMS500 electrical mobility size distribution to an aerodynamic size distribution and a volume equivalent size distribution.

In addition to the DMS500, Aethalometer, and APM, 13 samples were selected where the aerosol mass yields were corroborated by impactor measurements followed by gravimetric analysis. A four stage Dekati gravimetric impactor (DGI, Dekati Ltd., Kangasala, Finland) was used to sample particles on impactor plates. The lower cut-off diameters corresponded to 2.5, 1.0, 0.5, and 0.2  $\mu\text{m}$ . A filter was used to collect the remaining size fraction smaller than 0.2  $\mu\text{m}$ .

Two materials were selected for an analysis of elements susceptible to forming radionuclides. The elemental composition of the aerosols were analyzed with two different methods. The first method, inductively coupled plasma mass spectrometry (ICP-MS), was chosen to quantify mass fractions of specific elements of interest in the aerosol. The ICP-MS method thereby potentially allows calculation of the mass yield of specific elements in the aerosol phase that have been emitted during combustion of the material. The second method was high resolution transmission electron microscopy (HRTEM) combined with electron dispersive X-ray spectroscopy (EDX). This method allows identification of elements susceptible to forming radionuclides in single aerosol particles collected on a TEM substrate. Because aerosol particle composition often vary with particle size, this method can potentially deduce whether these elements are evenly distributed throughout the aerosol or are confined to certain particle sizes.

## 3.2 Aerosol sampling and set-up

The set-up for aerosol sampling, dilution and measurement is outlined in the subsections of this chapter. An overview of the set-up is presented in Figure 2.

### 3.2.1 Instrumentation

The instruments and the measured properties are listed in Table 1. The set-up included two instruments for highly time-resolved (1 s) particle characterization, and four instruments for off-line analysis and characterization of the full burn cycle.

The DMS500 (Cambustion, Cambridge, UK) was used to characterize the particle number size distribution and total particle number concentration in the size range 5-1000 nm. The DMS500 classifies particles according to their electrical mobility. Particles are first charged by a corona charger, and depending on their obtained charge state and particle size, they are deposited on and counted on an array of electrometers positioned at different distance from the classifier inlet. The obtained output particle size distribution depends on the choice of inversion matrix. The inversion matrix accounts for variations in charge distribution with particle size and morphology. For this study we used a soot inversion matrix initially derived for diesel soot aerosols that takes into account the agglomerated shape of soot particles.

Bimodal lognormal distributions were fit to the sample averaged particle number and mass yields. The distributions were fitted using nonlinear least squares minimization in MATLAB(R) (2018b). The fitting is sensitive to boundary and starting conditions and it is essential to visually verify the result in order to produce accurate bimodal lognormal distributions representative of the true aerosol distribution.

**Table 1. List of instruments.**

Instrument ID	Name	Characterization	Time-resolution
1	DMS500 (Cambustion)	Particle number size distribution	1s
2	Aethalometer (AE33, Magee Scientific)	Black carbon mass concentration	1s
3	DMA-APM-CPC (Kanomax USA, Inc.)	Particle mass and mass - mobility relationship	~10 min
4	Dekati gravimetric impactor (DGI, Dekati)	Particle mass size distribution	Full burn cycle
5	TSI Nanosampler (model 3089, TSI, Inc.)	TEM sample preparation using lacey carbon coated Cu grids	Full burn cycle
6	ICP-MS filter	ICP-MS sample preparation	Full burn cycle

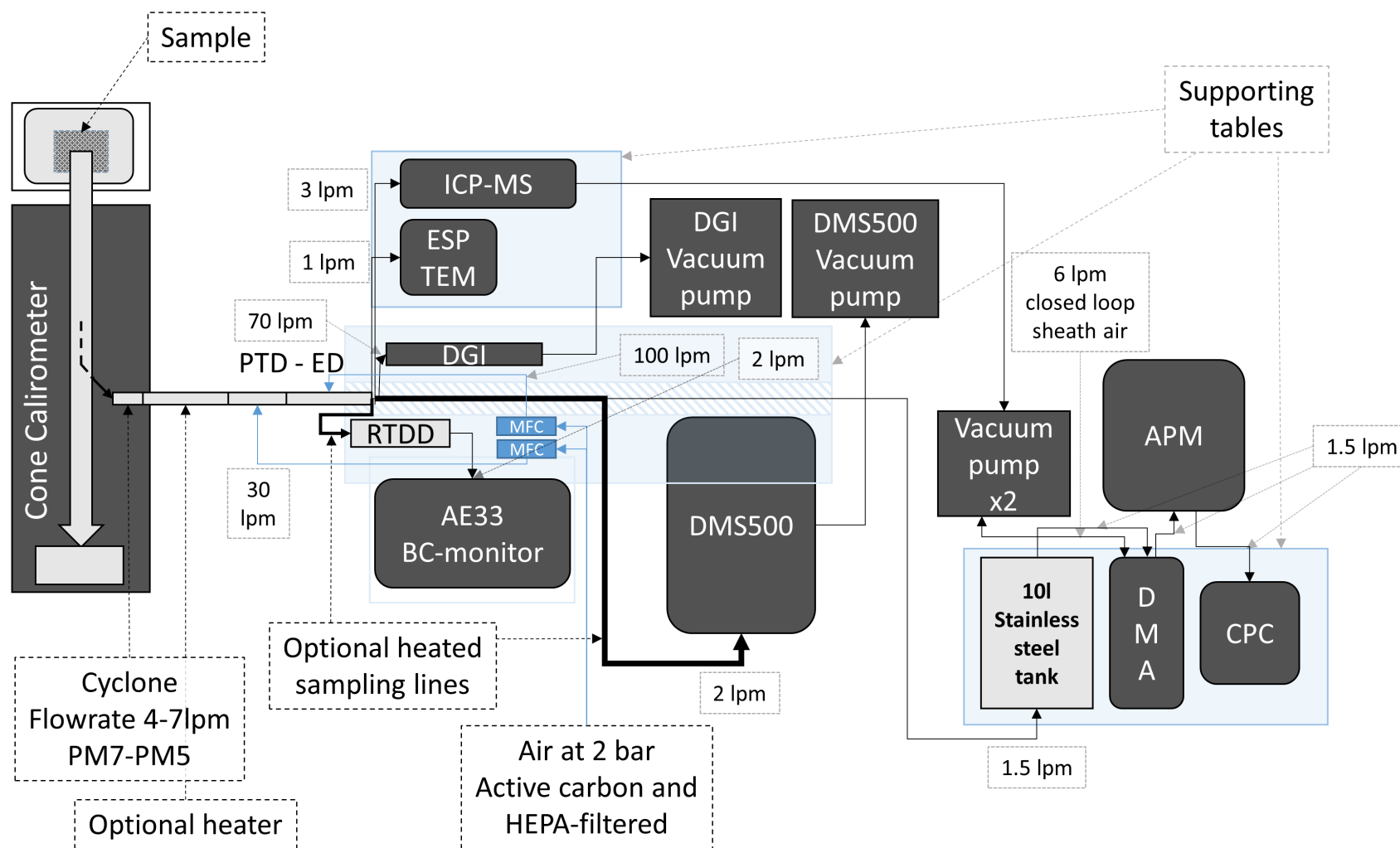


**Figure 2.** Set-up of the FIRIA aerosol characterization, view from above the set-up. The main instruments are further described in Table 1. PTD-ED is a Porous tube – ejector dilution system, RTDD is a rotating disc diluter supplying extra dilution to the BC monitor.

The aethalometer (model AE33, Magee Scientific, USA) was used to derive black carbon mass concentrations. The upper cut-off diameter was determined by the pre-cyclone ( $\sim 6\ \mu\text{m}$  for the flow rates used here). In the aethalometer, particles are deposited on a filter substrate and the light attenuation through the filter is measured. This allows for simple determination of black carbon equivalent mass concentrations. The AE33 operates at seven wavelengths using different LED's. The black carbon concentration is calibrated against elemental carbon mass and is commonly a good proxy for the highly absorbing solid fraction of the soot mass. We derived black carbon mass concentrations from the AE33 measurements performed at a wavelength of 880 nm.

The aerosol particle mass analyzer (APM) was used to derive the particle mass-mobility relationship and particle effective density. Particles were first size selected using a differential mobility analyzer (DMA), led through the APM, and counted in a condensation particle counter (CPC, TSI model 3075). This set-up is more correctly denoted DMA-APM-CPC, however we choose to refer to this set-up as simply the APM. Effective densities and particle mass-mobility relationships were evaluated at 50, 100, 150, and 300 nm (electrical mobility). The APM was calibrated at 100, 220, and 269 nm using polystyrene latex spheres with a density of  $1.05\ \text{g/cm}^3$ . We used the same calibration factor for 50 nm and 100 nm.

A Dekati gravimetric impactor (DGI) was operated at 70 lpm. It characterizes the particle mass size distribution based on aerodynamic equivalent diameter. The DGI includes four impactor stages with cut-off sizes at 2500, 1000, 500, and 200 nm, and a final filter for the remaining particle fraction smaller than 200 nm. The particles were collected on greased aluminum foils in the impactor stages, and on Emfab™ TX40HI20WW (Pallflex®) as the final filter. The aluminum foils and final filters were weighted before and after measurements and blank corrected using the average of two blanks.

Samples for ICP-MS were collected on cellulose filters prepared by the Division of Occupational and Environmental Medicine at Lund University. The ICP-MS analysis was conducted by ALS Scandinavia AB.

TEM samples were prepared by particle collection on lacey carbon coated Cu grids using an electrostatic precipitator (TSI Nanosampler model 3089). High-resolution TEM analysis was performed at the national center for high resolution electron microscopy (Lund University) and images acquired with a Gatan 2kx2k CCD camera and an exposure time of 1-2 s in a JEOL 3000F TEM, equipped with a Schottky FEG operated at 300 kV. The EDX was performed with the same microscope and the characteristic x-rays were detected by a silicon drift detector (SDD) Oxford XEDS detector. The Oxford software INCA was used in order to process the EDX data.

### **3.2.2 Primary aerosol dilution**

Instruments were connected at the outlet of the primary dilution stage. The primary dilution system (Venacontra aerosol diluter) consisted of a pre-cyclone (approximate cut-off size at  $6\ \mu\text{m}$ ), a steel tube with optional pre-heating, and a porous tube diluter (PTD) followed by an ejector diluter (ED). This system is referred to as PTD-ED and dilutes the aerosol using clean pressurized

air (air filtered through two stages of both HEPA- and active carbon filters) controlled by two mass flow controllers. The dilution in the ED was constant with a dilution factor of 4. The PTD was operated so that the total PTD-ED dilution factor was approximately 30. The dilution factor was monitored by simultaneous measurements of the CO<sub>2</sub> concentrations in the raw exhaust and in the diluted exhaust. With this set-up, the nominal flow rate of raw exhaust gases into the PTD-ED was 4-5 lpm at standard pressure and temperature, resulting in a total of approximately 130 lpm diluted aerosol exiting the PTD-ED. For the main tests, the primary dilution stage including the pre-cyclone and steel tube were operated without heating at ambient room conditions.

$$DF = \frac{CO_2^{Raw\ exhaust} - CO_2^{Raw\ background}}{CO_2^{Diluted\ exhaust} - CO_2^{Diluted\ background}} = \frac{\Delta CO_2^{Raw\ exhaust}}{\Delta CO_2^{Diluted\ exhaust}} \quad \text{Equation 1.}$$

The calculation of dilution factors (DF) is shown in equation 1 and an example for the primary dilution system over a full measurement is shown in Figure 3. The error increased sharply at steep  $\Delta CO_2$  gradients in the ignition and burnout combustion. This error was partly due to low CO<sub>2</sub> concentrations, and partly due to small off-sets in instrument times. The mean dilution factor was evaluated for CO<sub>2</sub> concentrations larger than 200 ppm in the duct (i.e., Cone calorimeter). We accounted for small natural fluctuations in the dilution factor, allowing a  $\pm 10\%$  fluctuation of the mean dilution factor. These natural variations may stem from fluctuations in gas temperature and pressures. Larger fluctuations in the calculated DF at steep  $\Delta CO_2$  gradients and at low CO<sub>2</sub> concentrations (<200 ppm CO<sub>2</sub> in the duct) were ignored and were instead substituted with the mean dilution factor.

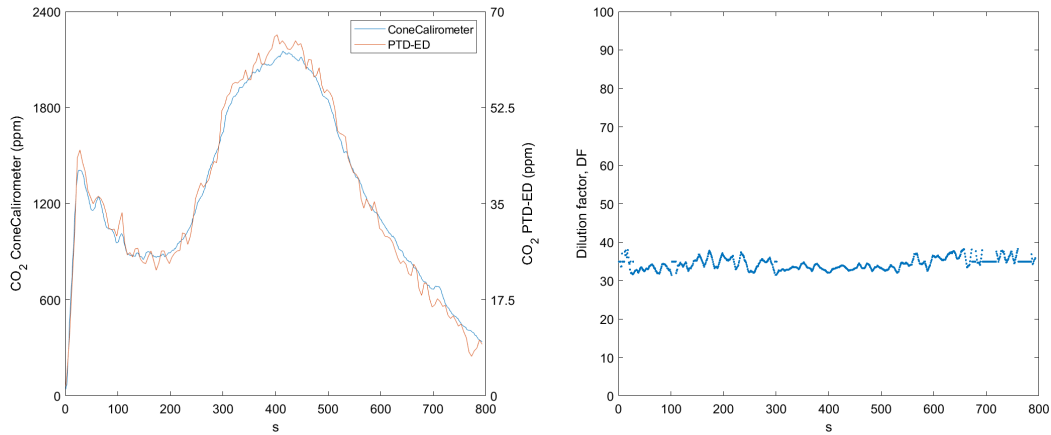


**Figure 3. Left:  $\Delta CO_2$  in raw exhaust (left axis) and after primary dilution (right axis) versus time in seconds. Right: Derived dilution factor (DF) for the same time period.**

### 3.2.3 Secondary aerosol dilution

Two secondary aerosol dilution systems were connected after the primary PTD-ED dilution system. These additional dilution systems were necessary to reduce particle concentrations to within operating concentrations of the DMS500 and Aethalometer. The DMS500 uses a built-in rotating disc diluter. The Aethalometer used a stand-alone rotating disc dilution system (TSI model 379020A) operating with essentially the same principles as the built-in dilution of the DMS500.

The systems have the option to dilute the aerosol at temperatures up to 150°C. This feature was not used for the main tests, and the aerosol was diluted at ambient room conditions.

### 3.3 Derivation of aerosol yield

The aerosol yield was derived by estimating the aerosol production per second (number or mass produced per second). The aerosol production per second was derived from the concentrations reported by the instruments (in units per volume of air) measured in diluted conditions, by consideration of primary and secondary dilution ratios, and by the constant flowrate in the cone calorimeter exhaust duct. At a given time, the aerosol concentration in the raw exhaust ( $C_{\text{duct}}$ ) is given by the aerosol concentration at diluted conditions ( $C_{\text{diluted}}$ ) multiplied by the total dilution factor ( $DF_{\text{total}}$ ) as shown in equation 2. The units differ between aerosol measurements and are therefore not included in equation 2.

$$C_{\text{duct}} = C_{\text{diluted}} \times DF_{\text{total}} \quad \text{Equation 2.}$$

The aerosol production per second is given by the aerosol concentration in the duct multiplied by the volumetric flow rate per second ( $Q_{\text{duct}}=0.024 \text{ m}^3/\text{s}$ ) (equation 3).

$$\text{Aerosol production} = C_{\text{diluted}} \times DF_{\text{total}} \times Q_{\text{duct}} \quad (\text{s}^{-1}) \quad \text{Equation 3.}$$

The aerosol yield (equation 4) can finally be derived by consideration of the mass loss rate from the sample ( $\Delta m_{\text{fuel}}$ ).

$$\text{Aerosol yield} = \frac{C_{\text{diluted}} \times DF_{\text{total}} \times Q_{\text{duct}}}{\Delta m_{\text{fuel}}} \quad (\text{g fuel}^{-1}) \quad \text{Equation 4.}$$

### 3.4 Estimating particle mass from combined DMS500 and APM measurements

The effective density provides a direct relationship between the particle mass and electrical mobility diameter,  $D_{\text{em}}$  (eq. 5).

$$\text{Mass}_{D_{\text{em}}} = \text{effective density}_{D_{\text{em}}} \times \text{Volume}_{D_{\text{em}}} \quad \text{Equation 5.}$$

Particle masses were obtained with the APM for particles selected with the DMA at 50, 100, 150, and 300 nm electrical mobility equivalent diameters. From these two numbers the effective density was calculated. Soot particles composed of fused monomers (primary particles) exhibit aggregated structures. The shape and size of soot particles therefore depend on the monomer sizes and number of soot monomers in the soot aggregate. The effective density of soot particles vs. mobility size is generally well described by a power law function. To interpolate the effective densities between the measured points and extrapolate outside the range of measured diameters, a power law function was fit to the measured effective densities at 100, 150, and 300 nm. The 50 nm point was excluded from the fit since the observed soot particle number mode was significantly larger than 100 nm. Particle effective densities between 50 and 100 nm were estimated by a spline fit of the soot density described by the power law function and the measured effective density at 50 nm. For a majority



of the measurements a strong nucleation mode was present. This nucleation mode is likely liquid in nature and composed of unburnt organic and inorganic combustion products which condense upon cooling in the duct and the primary dilution system. Therefore, we may not assume that the size dependence of effective densities will be described by the same power law function as soot densities. Particles with sizes below 50 nm were therefore assumed to have a constant effective density equal to the measured value at 50 nm.

The simultaneous knowledge of electrical mobility diameters and effective densities allowed us to derive particle aerodynamic diameters. The aerodynamic diameter is controlling sedimentation and inertial deposition, i.e. impaction. The procedure is described by Park et al. (2003) and shown in equation 6.

$$D_{ae} = D_{em} \sqrt{\frac{\rho_{eff} \times C_{em}}{\rho_0 \times C_{ae}}} \quad \text{Equation 6.}$$

In equation 5, the subscript “em” refers to electrical mobility and *ae* refers to aerodynamic.  $\rho_0$  is by definition equal to 1 (g/cm<sup>3</sup>) and the parameter  $\rho_{em}$  denotes the effective density for a given electrical mobility size.  $C_{em}$  and  $C_{ae}$  refer to the Cunningham slip correction factors for electrical mobility sizes and aerodynamic sizes respectively. The Cunningham slip correction factor (equation 7, Kulkarni et al. (2011)) depends on the particle diameter through the Knudsen number ( $Kn$ , equation 8).  $C_{em}$  can therefore be calculated directly from the DMS500 size information. On the other hand, the aerodynamic particle size ( $D_{ae}$ ) is not known and  $C_{ae}$  may not be calculated directly.

$$C_c = 1 + Kn(\alpha + \beta \times e^{-\gamma/Kn}) \quad \text{Equation 7.}$$

$$Kn = \frac{2\lambda}{D} \quad \text{Equation 8.}$$

$D_{ae}$  and  $C_{ae}$  (equation 6 and 7) were solved numerically by iteration. 50 iterations were used and is more than required to reach stable solutions at the given particle diameters. The constants  $\alpha$ ,  $\beta$ , and  $\gamma$  depend on particle properties. We used the parameterization for solid particles derived by Allen and Raabe (1985), where  $\alpha=1.142$ ,  $\beta=0.558$ , and  $\gamma=0.999$ .

Finally it should be pointed out the effective density should only be used when converting from or to electrical mobility diameters. When for example converting from mass to geometric volume the inherent material density should be used instead. It is ~1.8 g/cm<sup>3</sup> for pure elemental/black carbon (Park et al. 2004), while it is around 0.8 - 1.2 g/cm<sup>3</sup> for organic components with low oxygen content (as would be expected for most of the samples here) or 1.3-2.0 g/cm<sup>3</sup> for organic components with high O:C ratio.

## 4 Results and discussion

The FIRIA aerosol results are separated in four main parts. The first part presents an example of the primary analysis conducted in the post-processing of each sample. The second part contains a summary of the main aerosol parameters for all tests conducted. The third part contains the influence of vitiated air and heat flux on the results. The fourth part of the results section contains an error and sensitivity analysis.

In addition to the results and discussion presented in this report, the results of the primary analysis pertaining to all samples are available in the corresponding Microsoft Excel documents and associated folders. The processed time-resolved data was stored in tab delimited text (.txt) files. The figures are available in .png format and .fig formats (MATLAB<sup>®</sup>). Summary data with key-parameters for each sample, including average particle yields, were stored in a .xlsx format (Microsoft Excel). In addition: extraction times, time-adjustments, raw DMA-APM effective densities, and other parameters necessary for repeating the extraction procedure were stored in a separate Microsoft Excel document.

### 4.1 Presentation of the primary analysis

The post-processing and primary analysis were performed for all samples and included: time series of the evolution of aerosol yields (mass, number and BC) and aerosol size distributions over the experiment, average aerosol yields, evaluated mass-mobility diameter relation, average mass and number size distributions (electrical mobility and aerodynamic diameters) including bimodal lognormal fittings. Here we present the analysis for test number 22 (T22\_C04\_30\_1L\_US) as an example. Figures for all tests are available in separate folders (.png format and .fig MATLAB<sup>®</sup> format).

#### 4.1.1 Time-resolved processed test data

A summary is provided for each test according to Figure 4. The top graph of the summary includes the time history of DMS500 mass (soot) and number yields, and aethalometer BC yield. The second graph contains a comparison of the time-resolved DMS500 mass yield and the sum of CO and CO<sub>2</sub> concentration as proxy for the rate of combustion. The third graph shows time-integrated aerosol mass and BC yields. In this graph, the produced aerosol mass (g particles / s) and sample mass loss (g fuel/s) are integrated from t=1s to any given time during the experiment. The final value at the end of the experiment is thus equal to the aerosol yield of the full experiment (presented in Table 2). The fourth graph shows the  $\Delta\text{CO}_2$  concentration in the duct (Cone Calorimeter) and after dilution (PTD-ED). This graph is included as a verification of the aerosol sampling.

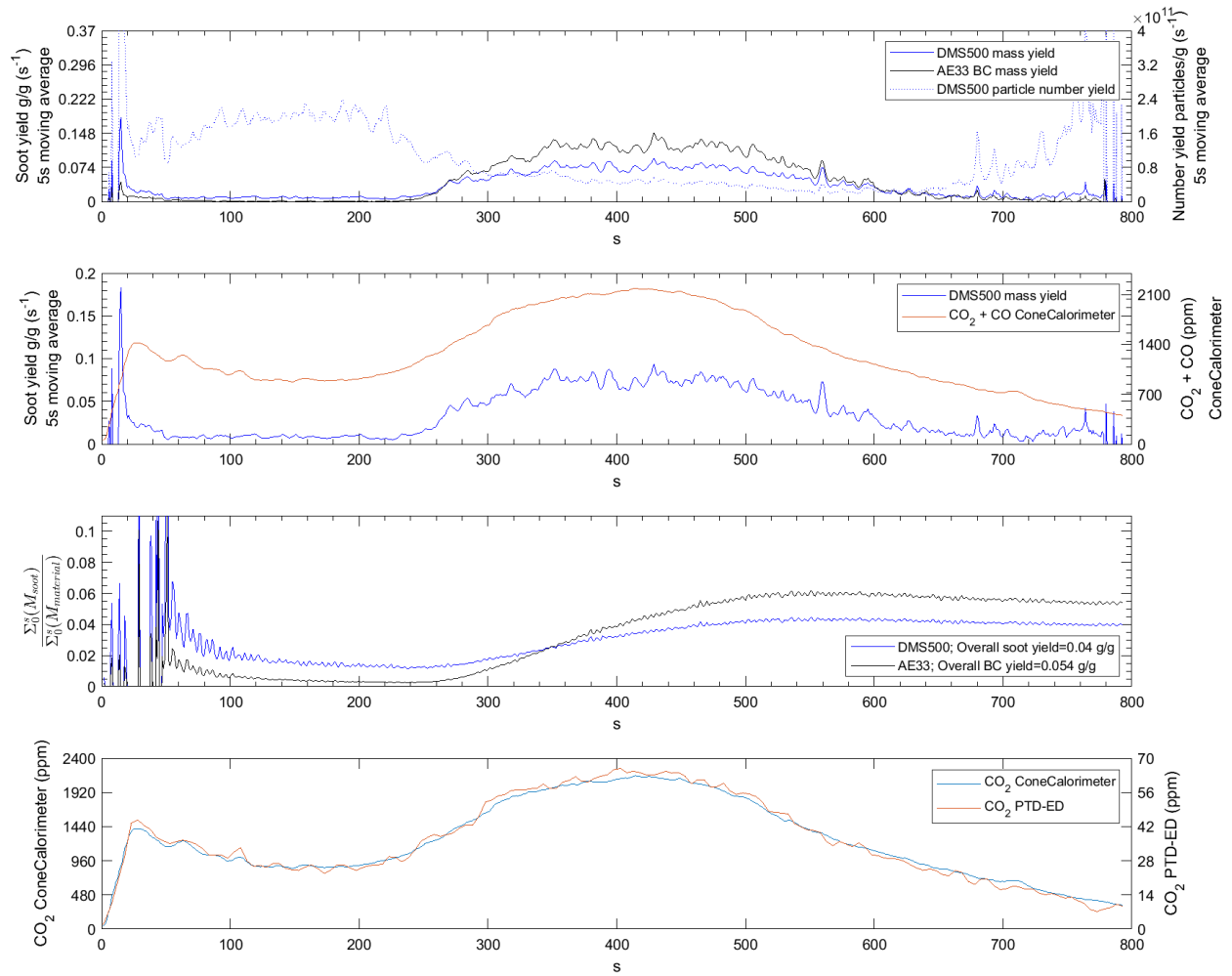


**Figure 4. Time-resolved aerosol number, mass and BC yields (top). Time-resolved mass yield and sum of CO and CO<sub>2</sub> flue gas concentrations (second from top). Time-integrated aerosol mass and BC yields (third from top). CO<sub>2</sub> concentrations in flue gases and after primary dilution (bottom).**

In addition to the summary presented in Figure 4, time traces of the dilution factor (Figure 3), DMS500 mass and BC aerosol emissions (Figure 5), and particle number and mass size distributions (Figure 6) are also available from the primary analysis.

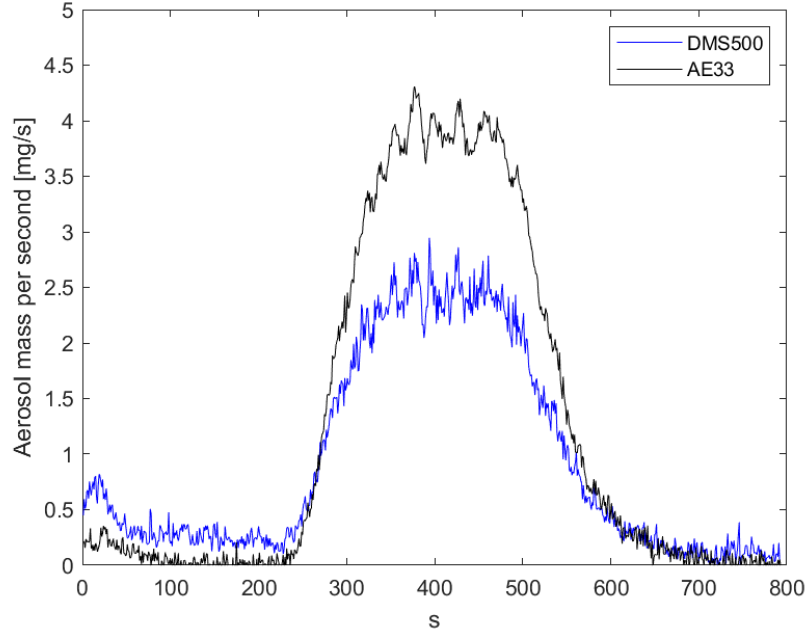


**Figure 5. Time-trace of aerosol mass and BC production.**

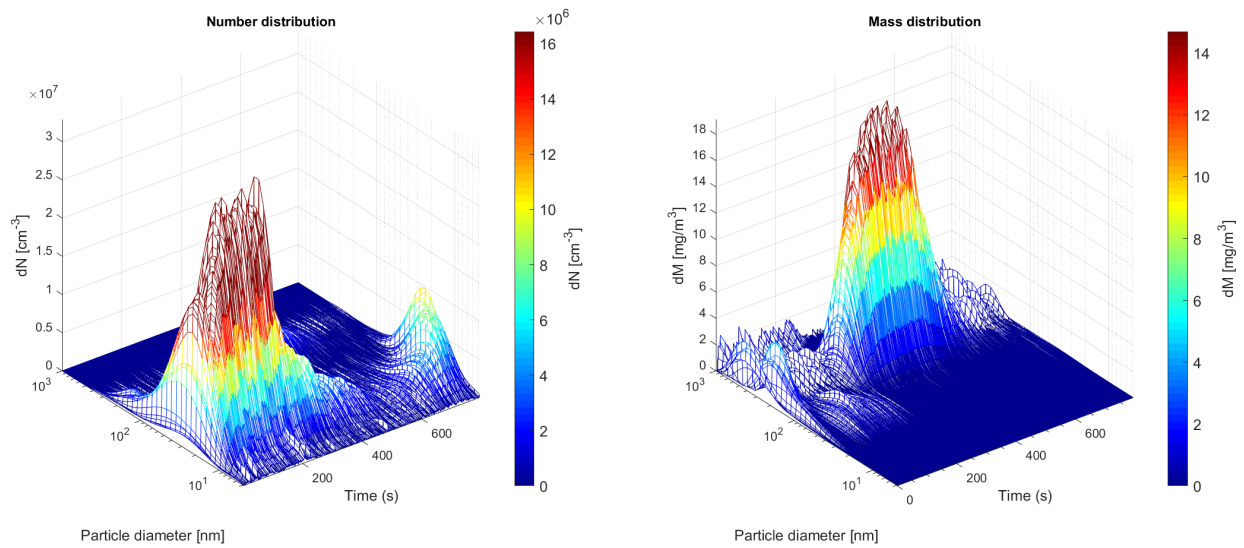


**Figure 6. Time-trace of aerosol number (left) and mass (right) size distributions.**

#### 4.1.2 Reduction of the results into a simplified model using bimodal lognormal distribution fitting

Bimodal lognormal distribution functions were fit to the number size distribution data from the DMS500. The bimodal distribution fitting contains two modes: one nucleation mode and one accumulation mode. Each fitted size distribution can be described by three parameters, the geometric mean diameter (GMD), the geometric standard deviation (GSD), and the total number concentration of particles. The number size distribution was converted to a mass weighted size

distribution using parameterizations of the effective density as a function of mobility size (section 4.1.3). Figure 7 presents examples of the averaged size distributions with lognormal fits. Parameter estimates for the lognormal distributions are shown in the inset of Figure 7. The fitting was conducted for aerosol size distributions of both electrical mobility diameters and after first converting to aerodynamic diameters using Eq. 6.

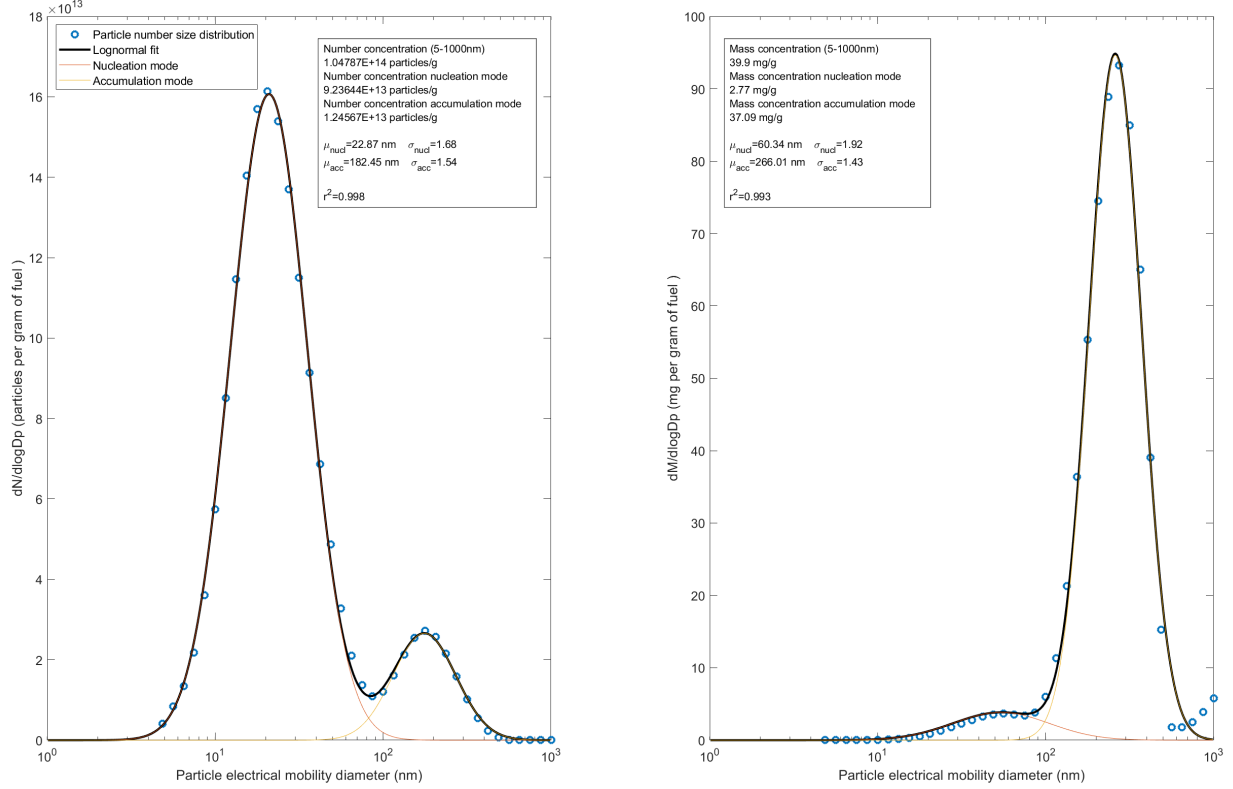


**Figure 7. Averaged aerosol size distributions and bimodal lognormal fittings. The fitted parameters are shown in the insets.**

In addition to the number and size distributions obtained from the DMS500 data, bimodal lognormal fittings were also performed for the DGI mass size distribution data for the samples when impactor sampling was conducted. An example of the DGI mass size distribution with bimodal lognormal distribution fitted is shown in Figure 8. In this case a single size mode was fit to the data in the sub micrometer range. This size mode essentially corresponds to the accumulation mode as this mode commonly dominates the mass strongly. Additionally, the impactor classifies particle size by aerodynamic diameter, which causes a decreased difference between the two original size modes due to the low effective density of soot agglomerates in the accumulation mode. Finally, the resolving power of the impactor is not high enough to separate modes that are close in peak diameter.

In this case we instead fitted a coarse mode for particles larger than one micrometer, this may correspond to larger ash particles emitted directly from the remaining solid material in the sample, a previously observed in biomass combustion (Pagels et. al 2003), when high flow rates through

the grate are applied. However, this size mode was only corresponding to a minor part of the total mass in this study, as is commonly the case for combustion emissions such as diesel exhaust and small-scale biomass combustion. Coarse particles have a limited range due to their high sedimentation velocity. For example a 10  $\mu\text{m}$  particle settles 1 m in six minutes. Therefore particles above 10  $\mu\text{m}$  can only reach a very limited distance from the source and are of limited relevance.

This taken together with the observed low mass fractions in the coarse mode suggests that the undetected mass fraction between the 50% cut off diameter of the cyclone in the dilution system, 6  $\mu\text{m}$  and 10  $\mu\text{m}$  is only a small fraction of the total mass, perhaps less than 5-10%.

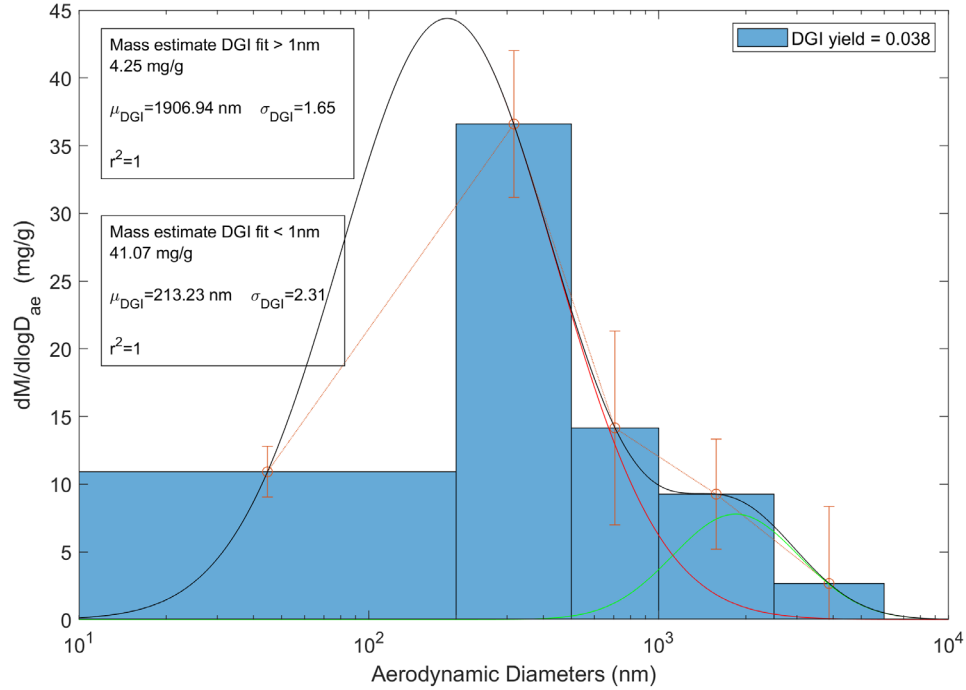


**Figure 8. DGI mass size distribution and bimodal lognormal fitting. Parameter estimates are shown in the insets.**

#### 4.1.3 Effective density distribution

In addition to the previously reported figures, the primary analysis also includes a figure of the effective density distribution used in the evaluation of the current tests. The effective density distribution was interpolated between 50-300 nm, and extrapolated down to 5 nm and up to 1000 nm in order to comply with the electrical mobility size distributions obtained from the DMS500. Figure 9 shows the effective density distribution used for the current example, notice the constant values at diameters <50 nm. The applied effective density distributions were based on APM measurements as discussed in detail in section: 4.2.3.

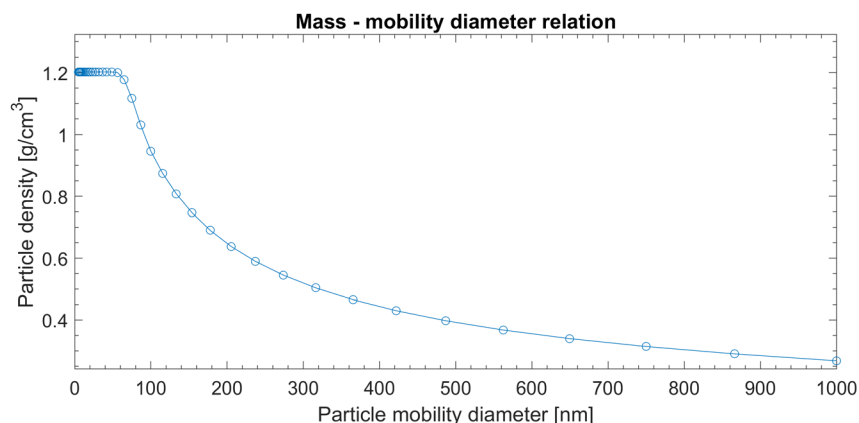


**Figure 9. Effective density distribution.**

## **4.2 Concluding summary of aerosol mass, BC, and particle number yields**

### **4.2.1 Aerosol yields**

Aerosol mass, number and BC yields were derived for all samples. Figure 10 presents the aerosol mass and BC yields sorted by the DMS500 mass yield. Tabulated values including particle number yields are available in Table 2. The total range of aerosol mass yields spanned from approximately 0.23 (g/g fuel) in the high end, to 0.005 (g/g fuel) in the low end. In summary, the highest aerosol mass yields (~0.10-0.23 g/g fuel) were obtained for electrical components (i.e., printed circuit boards), plastic components, oil, and magnets. Cables were represented at aerosol mass yields lower than 0.10 (g/g fuel). The effect on aerosol yields from incident heat flux and vitiated combustion is discussed in section 4.3.

Gravimetric measurements with the DGI were conducted for 13 experiments. The aerosol mass yields for the samples where the DGI was included ranged from approximately 0.15 down to 0.02 gram of aerosol particles per gram of fuel (g/g fuel). The mass yields derived from the on-line measurements of size distributions with the DMS500 are corroborated by the good agreement to independent measurements and mass yields obtained for the DGI (see discussion in section 4.4.3).

The particle number yields presented in Table 2 spanned two orders of magnitude, from approximately  $0.05 \times 10^{14}$  to  $2 \times 10^{14}$  emitted particles per gram of fuel (#/g fuel). The total particle number yield represents the sum of nucleation mode and accumulation mode particles in the DMS500 size range 5-1000 nm. The accumulation mode particles were the main contributors to the aerosol mass yields while the low mass of small nucleation mode particles contributed little to the aerosol mass yields. The average geometric mean diameter (GMD) of the number weighted accumulation mode (electrical mobility) was 159.0 nm (std of 55.1 nm) while the average GMD of the mass weighted accumulation mode was 269.0 nm (std of 84.1 nm).

Black Carbon (BC) yields were mostly of similar magnitudes to mass yields and BC was closely related to the presence of accumulation mode particles. However, the absence of BC was not identified as synonymous to the absence of an accumulation mode. This indicates that for at least some samples, low- and semi-volatile pyrolysis compounds with low light absorption dominated

the aerosol mass yields and may have dominated the accumulation mode. The partitioning between the gas and particle phase of such compounds is temperature dependent. In addition, nucleation mode particles in combustion derived aerosols generally form when flue gases cool and condensable vapors nucleate to form new particles. It was therefore of interest to estimate the aerosol yield of nucleation mode particles in relation to the dilution conditions. In addition to the normal test procedure, cable 04 was tested with the PTD-ED dilution gas heated to approximately 150°C, and the cyclone pre-heated to 250°C. In this experiment, the sampling line to the DMS500 was also heated to 150°C. Heating the dilution gas and sampling lines resulted in a reduction of the nucleation mode particle number in relation to the accumulation mode particle number. Nonetheless, the high temperature sampling conditions did not remove the nucleation mode, and the nucleation mode number yield still contributed significantly to the total aerosol number yield. We therefore conclude that the conservative estimate of the aerosol number yield is represented by cold dilution (used for all tests).



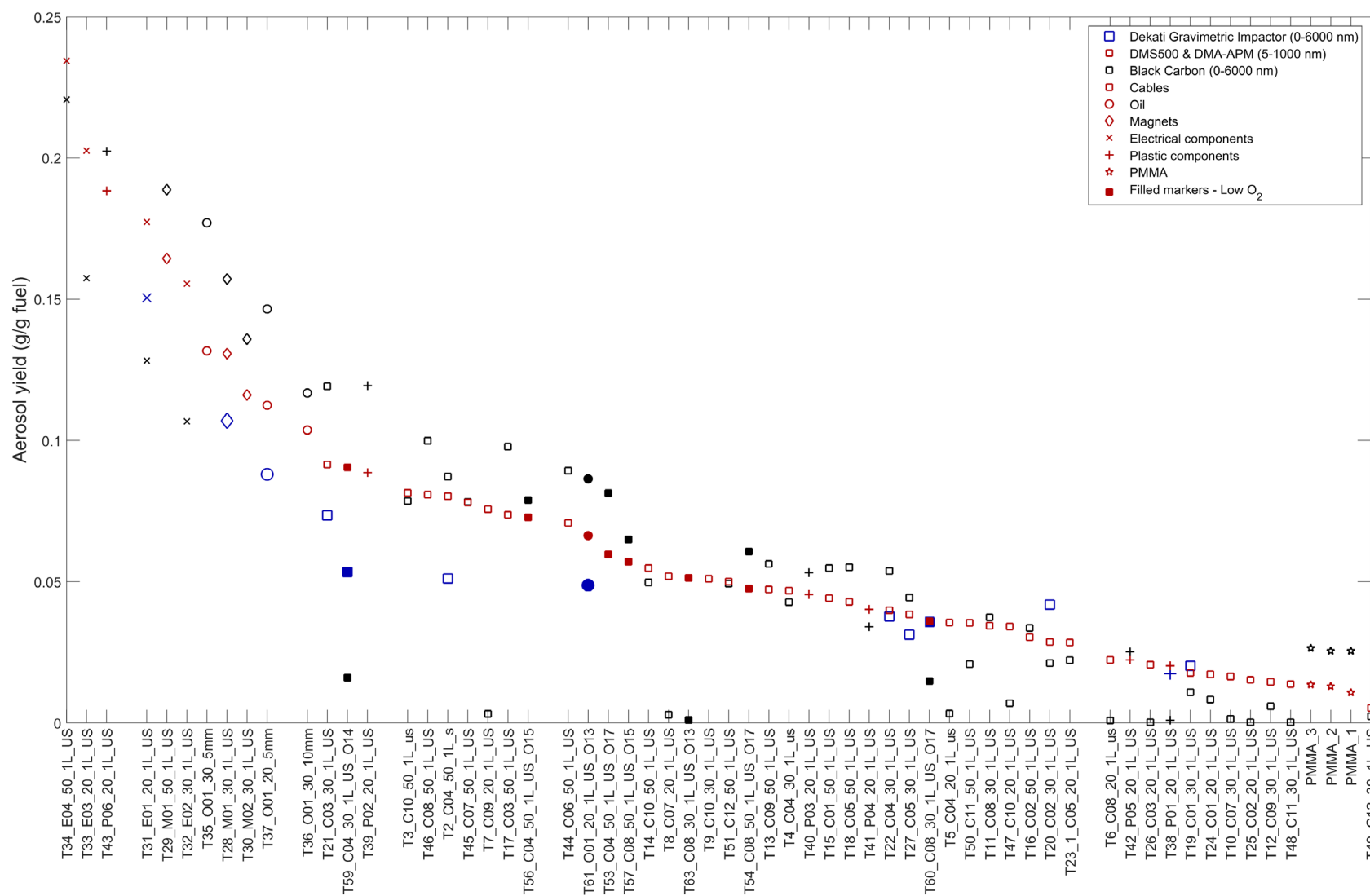


**Figure 10. Main summary of aerosol mass yields.**

**Table 2. Summary of analysis. Aerosol yields of mass, BC, and particle number derived for DGI, DMS500, and AE33 measurements. DGI measurements are highlighted in bold. The table is sorted by the DMS500 mass yield.**

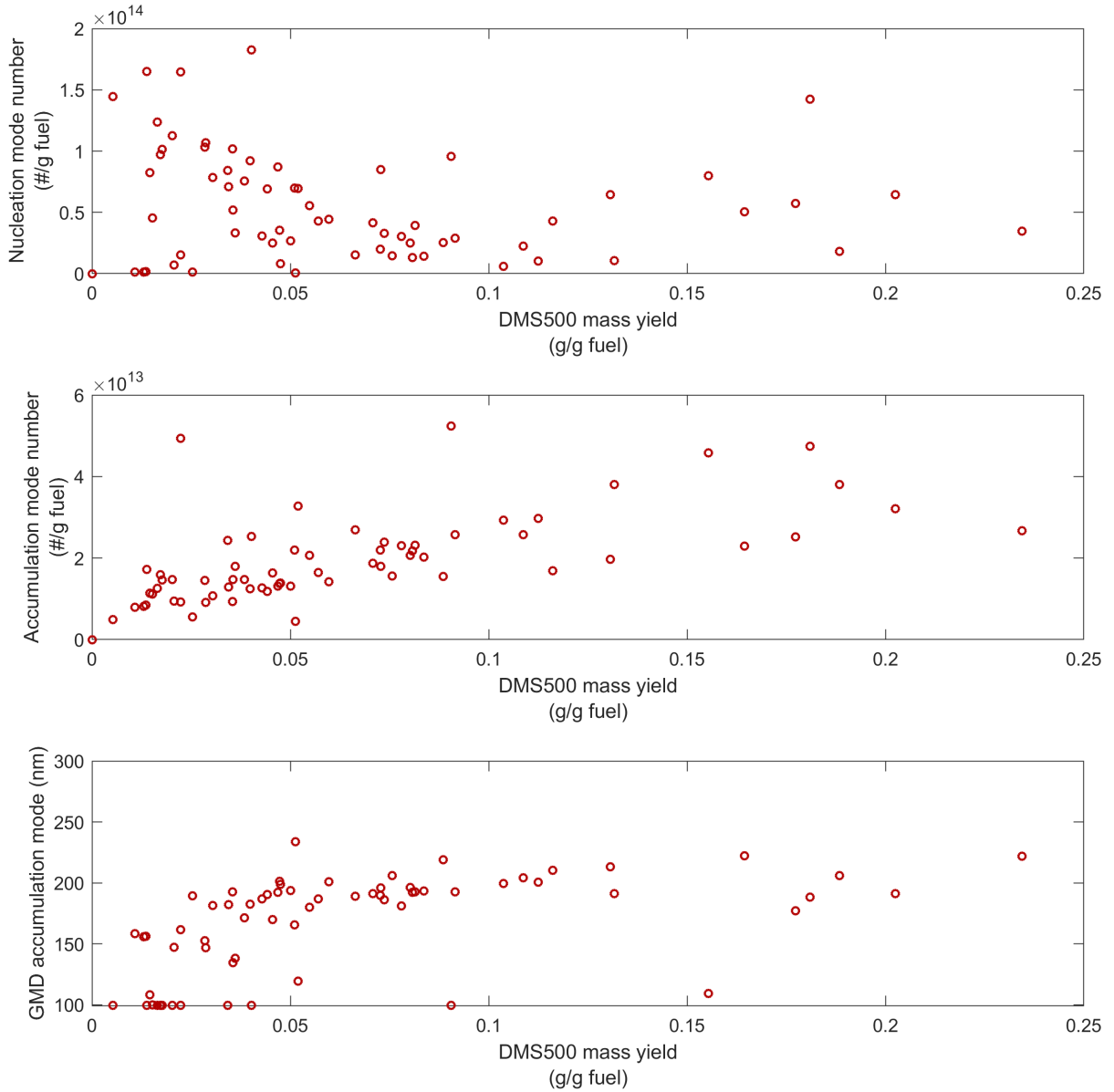
Test ID	Sample	Effect (kW/m <sup>2</sup> )	Test condition	DGI mass yield (g/g fuel)	DMS500 mass yield (g/g fuel)	AE33 BC yield (g/g fuel)	DMS500 number yield (#/g fuel)
34	E04	50	Normal		0.234	0.221	6.16E+13
33	E03	20	Normal		0.203	0.157	9.66E+13
43	P06	20	Normal		0.188	0.202	5.58E+13
<b>31</b>	<b>E01</b>	<b>20</b>	<b>Normal</b>	<b>0.150</b>	<b>0.177</b>	<b>0.128</b>	<b>8.44E+13</b>
29	M01	50	Normal		0.164	0.189	7.23E+13
32	E02	30	Normal		0.155	0.107	1.30E+14
35	O01	30	Normal		0.132	0.177	4.80E+13
<b>28</b>	<b>M01</b>	<b>30</b>	<b>Normal</b>	<b>0.107</b>	<b>0.131</b>	<b>0.157</b>	<b>8.40E+13</b>
30	M02	30	Normal		0.116	0.136	5.90E+13
<b>37</b>	<b>O01</b>	<b>20</b>	<b>Normal</b>	<b>0.088</b>	<b>0.112</b>	<b>0.147</b>	<b>3.99E+13</b>
36	O01	30	Normal		0.104	0.117	3.51E+13
<b>21</b>	<b>C03</b>	<b>30</b>	<b>Normal</b>	<b>0.073</b>	<b>0.092</b>	<b>0.119</b>	<b>5.45E+13</b>
<b>59</b>	<b>C04</b>	<b>30</b>	<b>Vitiated 14% O<sub>2</sub></b>	<b>0.053</b>	<b>0.090</b>	<b>0.016</b>	<b>1.49E+14</b>
39	P02	20	Normal		0.089	0.119	4.03E+13
3	C10	50	Normal		0.081	0.079	6.20E+13
46	C08	50	Normal		0.081	0.100	3.45E+13
<b>2</b>	<b>C04</b>	<b>50</b>	<b>Normal</b>	<b>0.051</b>	<b>0.080</b>	<b>0.087</b>	<b>4.54E+13</b>
45	C07	50	Normal		0.078	0.078	5.27E+13
7	C09	20	Normal		0.076	0.003	2.98E+13
17	C03	50	Normal		0.074	0.098	5.63E+13
56	C04	50	Vitiated 15% O <sub>2</sub>		0.073	0.079	1.02E+14
44	C06	50	Normal		0.071	0.089	5.97E+13
<b>61</b>	<b>O01</b>	<b>20</b>	<b>Vitiated 13% O<sub>2</sub></b>	<b>0.049</b>	<b>0.066</b>	<b>0.086</b>	<b>4.21E+13</b>
53	C04	50	Vitiated 17% O <sub>2</sub>		0.060	0.081	5.88E+13
57	C08	50	Vitiated 15% O <sub>2</sub>		0.057	0.065	5.96E+13
14	C10	50	Normal		0.055	0.050	7.54E+13
8	C07	20	Normal		0.052	0.003	1.02E+14
63	C08	30	Vitiated 13% O <sub>2</sub>		0.051	0.001	4.99E+12
9	C10	30	Normal		0.051	0.051	9.05E+13
51	C12	50	Normal		0.050	0.049	3.97E+13

Table 2 Continued.

54	C08	50	Vitiated 17% O <sub>2</sub>		0.048	0.061	2.22E+13
13	C09	50	Normal		0.047	0.056	4.95E+13
4	C04	30	Normal		0.047	0.043	9.94E+13
40	P03	20	Normal		0.045	0.053	4.11E+13
15	C01	50	Normal		0.044	0.055	8.07E+13
18	C05	50	Normal		0.043	0.055	4.34E+13
41	P04	20	Normal		0.040	0.034	2.26E+14
<b>22</b>	<b>C04</b>	<b>30</b>	<b>Normal</b>	<b>0.038</b>	<b>0.040</b>	<b>0.054</b>	<b>1.05E+14</b>
<b>27</b>	<b>C05</b>	<b>30</b>	<b>Normal</b>	<b>0.031</b>	<b>0.038</b>	<b>0.044</b>	<b>9.04E+13</b>
<b>60</b>	<b>C08</b>	<b>30</b>	<b>Vitiated 17% O<sub>2</sub></b>	<b>0.036</b>	<b>0.036</b>	<b>0.015</b>	<b>5.06E+13</b>
5	C04	20	Normal		0.035	0.003	6.66E+13
50	C11	50	Normal		0.035	0.021	1.11E+14
11	C08	30	Normal		0.034	0.037	8.37E+13
47	C10	20	Normal		0.034	0.007	1.09E+14
16	C02	50	Normal		0.030	0.034	8.81E+13
<b>20</b>	<b>C02</b>	<b>30</b>	<b>Normal</b>	<b>0.042</b>	<b>0.029</b>	<b>0.021</b>	<b>1.15E+14</b>
23	C05	20	Normal		0.028	0.022	1.17E+14
67	C08	30	Vitiated 15% O <sub>2</sub>		0.025	0.001	6.96E+12
6	C08	20	Normal		0.022	0.001	2.27E+14
42	P05	20	Normal		0.022	0.025	2.50E+13
26	C03	20	Normal		0.021	0.000	1.64E+13
<b>38</b>	<b>P01</b>	<b>20</b>	<b>Normal</b>	<b>0.017</b>	<b>0.020</b>	<b>0.001</b>	<b>1.27E+14</b>
<b>19</b>	<b>C01</b>	<b>30</b>	<b>Normal</b>	<b>0.020</b>	<b>0.018</b>	<b>0.011</b>	<b>1.15E+14</b>
24	C01	20	Normal		0.017	0.008	1.13E+14
10	C07	30	Normal		0.016	0.001	1.35E+14
25	C02	20	Normal		0.015	0.000	5.66E+13
12	C09	30	Normal		0.015	0.006	9.44E+13
48	C11	30	Normal		0.014	0.000	1.95E+14
70	PMMA	75	Reference		0.014	0.026	1.00E+13
69	PMMA	75	Reference		0.013	0.025	9.20E+12
68	PMMA	75	Reference		0.011	0.026	9.23E+12
49	C12	30	Normal		0.005	0.002	1.49E+14

#### 4.2.2 Evaluation of relationships between particle number, mass, and BC yields

There was no direct connection between aerosol mass yield and the *total* aerosol number yield. For the majority of combustion aerosols we observed two particle modes, one nucleation mode with mean diameters in the range 10-50 nm and one accumulation mode with diameters in the range 90-300 nm. The aerosol mass yields were associated with increasing number of accumulation mode particles and increasing geometric mean diameter of the accumulation mode (Figure 11). Conversely, Figure 12 shows that the aerosol number yields were mainly determined by an increasing number of nucleation mode particles ( $r^2=0.95$ ), and characterized by a small geometric mean diameter of both nucleation mode and accumulation mode particles.



**Figure 11. Aerosol mass yield (DMS500) versus the nucleation mode number concentration (top), accumulation mode number concentration (middle), and geometric mean diameter of the accumulation mode particle size distribution (GMD, bottom).**

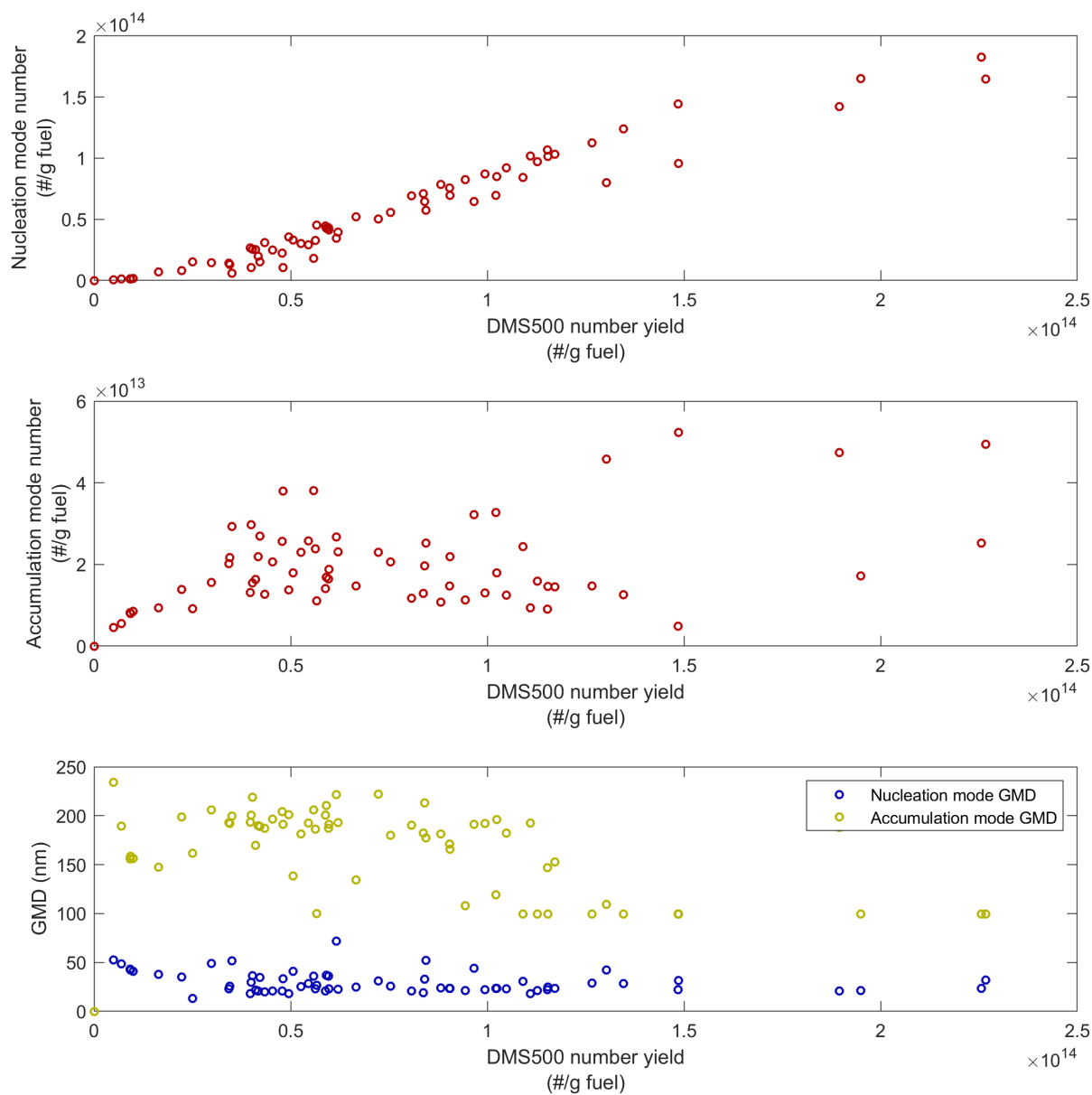


**Figure 12. Aerosol number yield (DMS500) versus the nucleation mode number concentration (top), accumulation mode number concentration (middle), and geometric mean diameter for both nucleation and accumulation mode particle size distributions (GMD, bottom).**

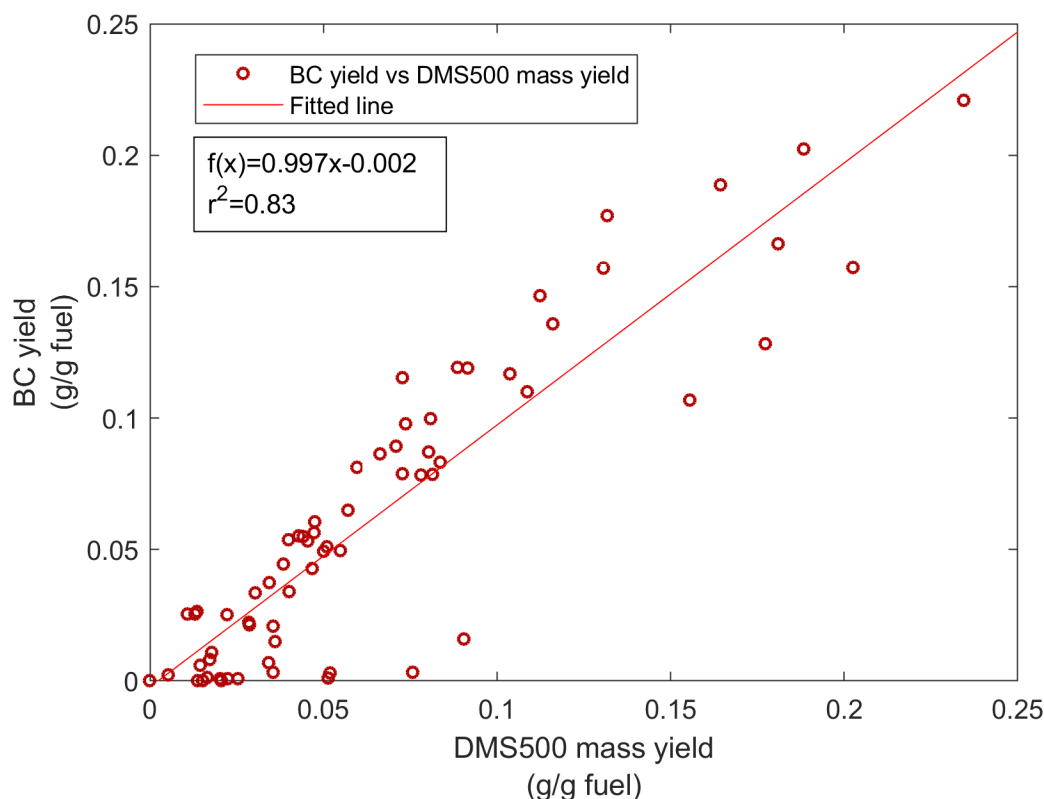


**Figure 13. BC yields from aethalometer absorption data versus mass yields derived from DMS500 size distributions and DMA-APM effective density distributions.**

The BC yield was closely related to the DMS500 mass yield ( $r^2=0.83$ , Figure 13). The variability in the scatterplot of Figure 13 is explained by BC being dependent on both the total particle mass and the aerosol optical properties. It is important to note that for some of the samples presented in Figure 10, BC appear very low in comparison to mass yields calculated for the DMS500 and DGI. This phenomena was observed for samples combusted at low heat fluxes ( $20 \text{ kW/m}^2$ ) and during vitiated combustion. The aerosol produced at these conditions thus appear to be low or non-absorbing (transparent). The presence of large particles may still cause significant light extinction and visibility reductions due to scattering.

#### **4.2.3 Evaluation of particle mass and effective density**

Particle mass was assessed using the APM, and effective densities were derived for particles of mobility sizes at 50, 100, 150, and 300 nm (pre-classified with a DMA). Particle mass and effective densities were evaluated for a total of 33 tests. Figure 14 and Table 3 summarizes the results of the APM measurements. These results are instrumental for the derivation of particle mass from the DMS500 by relating particle mass to a given electrical mobility size. Cables and oil in particular exhibited effective density distributions characteristic of soot dominated aerosols with agglomerated particle structures. A typical effective density distribution for diesel soot is included for reference in Figure 14 (left). For the tests where the APM was used to classify magnets and

electrical components, effective densities appeared characteristic of more spherically shaped particles.

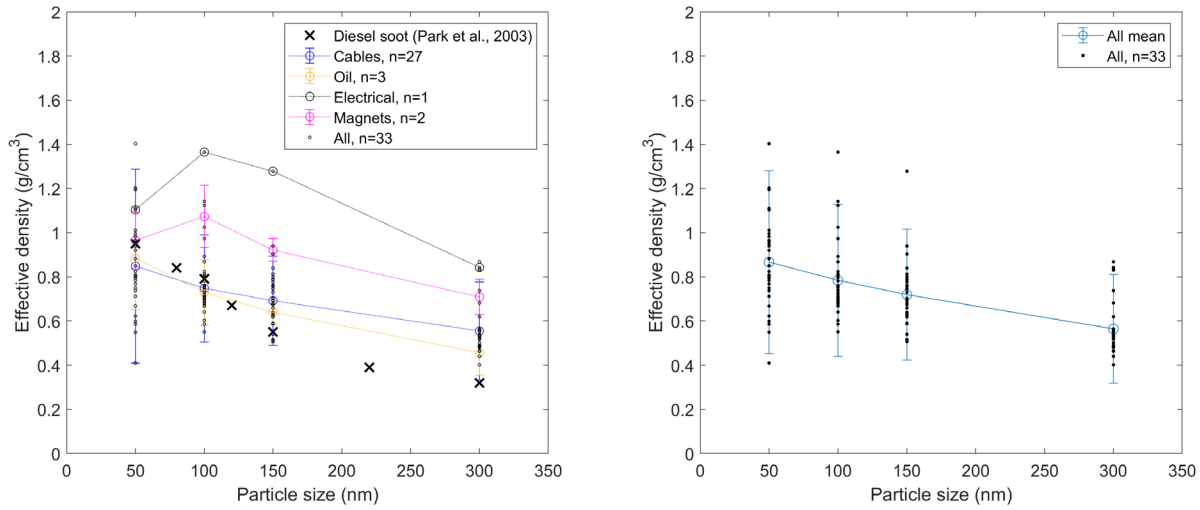


**Figure 14.** Summary of effective densities determined with the DMA-APM. Black dots indicate individual measurements and the circles connected by dotted lines indicate averages for each group of combustibles (left) and average of all combustibles (right). Black crosses shows typical effective densities for diesel soot (Park et al., 2003). Error bars show  $\pm 2$  standard deviations, the number of measurements are included in the figure legend.

When APM measurements were not conducted for a particular sample of cables, magnets, or oil, effective densities were assigned the averages derived for each group of combustibles (Figure 14, left). When APM measurements were not conducted for a particular sample of electrical components, effective densities were instead assigned from the average of both electrical components and magnets. For the group of *plastic* combustibles no APM measurements were conducted. For this group we assigned effective densities from the average of all APM measurements (Figure 14, right).

**Table 3.** APM effective density measurements of average values and standard deviations (right columns) for particles with 50, 100, 150, and 300 electrical mobility diameter. The number of measurements (N) is summarized on the last row.

Size (nm)	All (g/cm <sup>3</sup> )		Cables (g/cm <sup>3</sup> )		Oil (g/cm <sup>3</sup> )		Electrical (g/cm <sup>3</sup> )		Magnets (g/cm <sup>3</sup> )	
50	0.75	0.19	0.72	0.19	0.88	0.12	1.10	-	0.82	0.05
100	0.68	0.17	0.64	0.10	0.73	0.07	1.36	-	0.92	0.06
150	0.63	0.15	0.59	0.09	0.64	0.03	1.28	-	0.79	0.02
300	0.56	0.12	0.56	0.11	0.46	0.05	0.84	-	0.71	0.04
N	33		27		3		1		2	

## 4.3 Effect of heat flux and vitiated combustion

### 4.3.1 Heat flux

The effect of varying the incident heat flux to the samples is presented in two parts. Figure 15 shows the DMS500 mass yields and AE33 BC yields of cable 04 for different incident heat fluxes. Figure 15 also gives insight into the repeatability in measured yields for two identical tests at 30 kW/m<sup>2</sup> conducted on different days. In Figure 15 we observe a tendency for increasing mass and BC yields with increasing heat fluxes, in particular for the BC yields. The increase in mass yields at higher heat fluxes appear to be related to increased formation of soot particles. The substantial aerosol mass yield but negligible BC yield at 20 kW/m<sup>2</sup> indicates that other, non-BC low volatility pyrolysis products may dominate the aerosol for these cases.

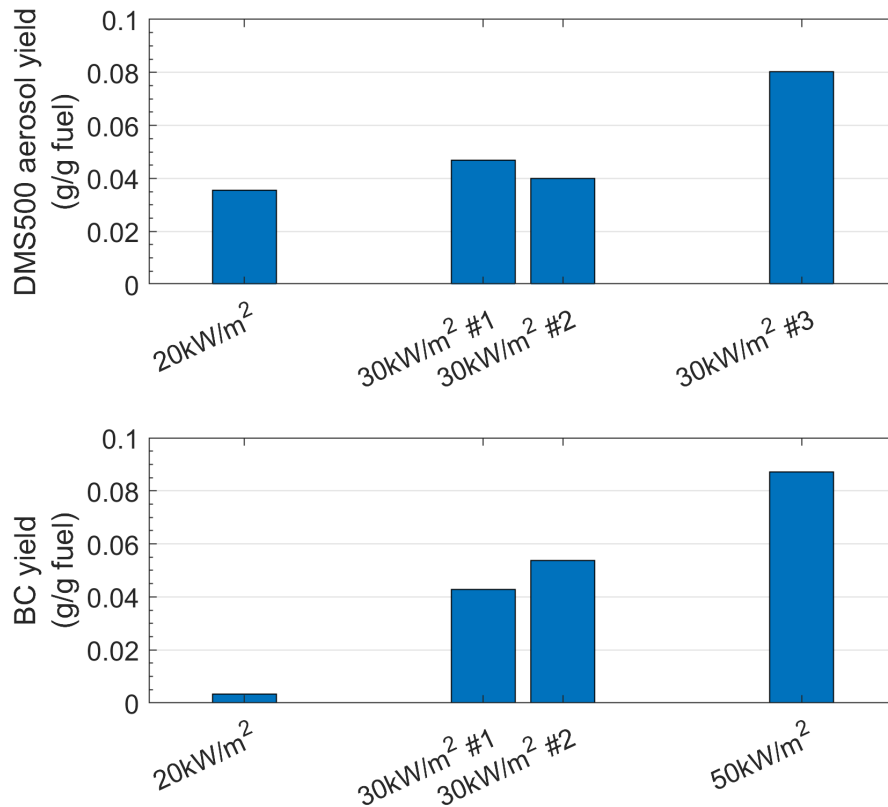


**Figure 15. Aerosol mass yield (DMS500) and BC yield (AE33) for cable 04 and increasing incident heat flux. The two tests at 30 kW/m<sup>2</sup> were performed on different days and represent an indication of the repeatability.**

Most of the cables (C01, C02, C03, C04, C05, C07, C08, C09, C10, C11, and C12) as well as a magnet (M01) and the oil (O01) were tested at different incident heat flux. The mass and BC yields for all these samples at a heat flux of 20, 30, and 50 kW/m<sup>2</sup> are shown in Figure 16. The median values at each heat flux have been indicated by squares. Although the data points presented in Figure 16 are not paired, they illustrate an increase in aerosol mass and BC yields for increasing heat flux. The analysis using paired data (i.e., the effect of heat flux for each material) was



consistent with the results presented in Figure 16, and showed positive coefficients to all linear fits (increasing yield for higher heat flux values) with only a few exceptions.

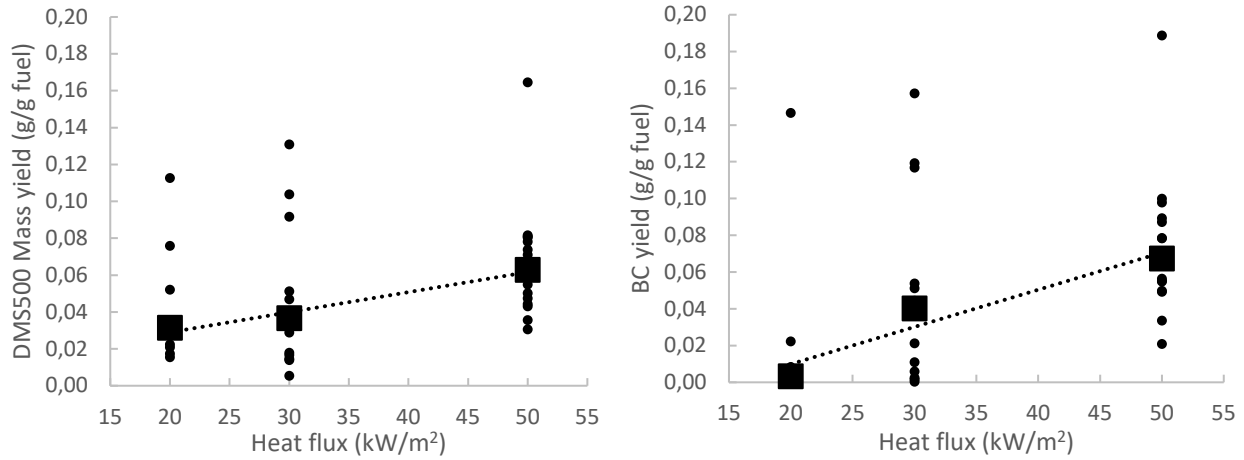


**Figure 16.** Effect of incident heat flux on aerosol mass yield (left) and BC yield (right). Squares represent median values for which linear trend lines have been fitted to assist the eye.

#### 4.3.2 Vitiated combustion

The effect on aerosol yields from combustion in vitiated air is shown in Figure 17. The most prominent effect of vitiated air was a strong reduction in BC yields for all three sample materials.

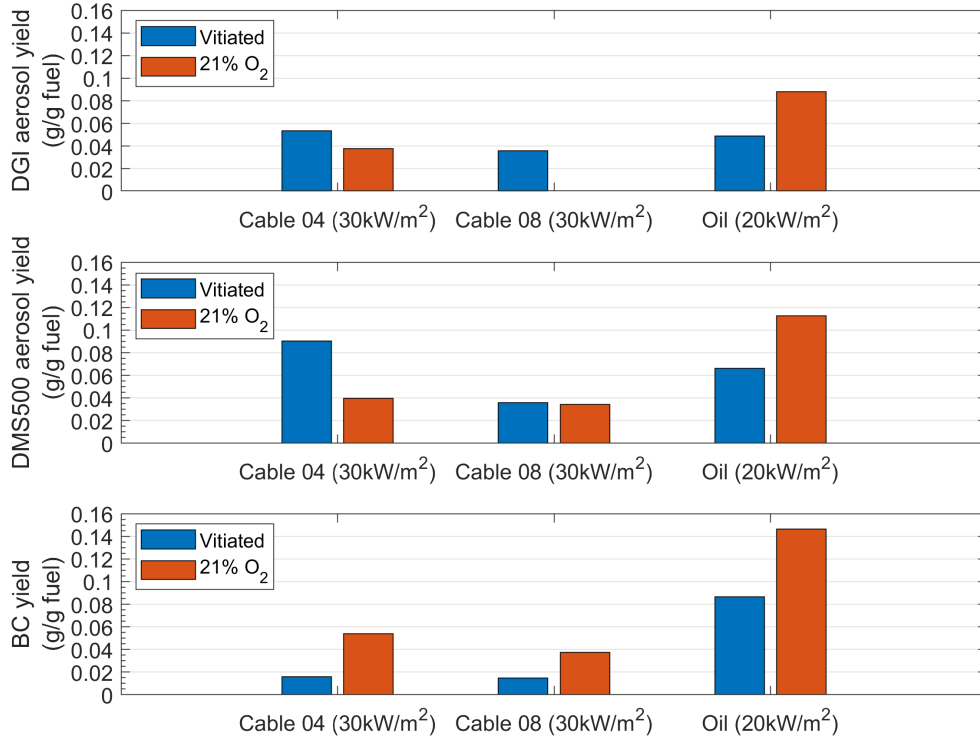


**Figure 17.** Aerosol mass yields (DGI and DMS500) and BC yields for vitiated combustion and combustion at normal condition (21% O<sub>2</sub>) conducted at a heat flux of 30 kW/m². Data refers to test numbers: 22 and 59 (cable 04), 11 and 60 (cable 08), 37 and 61 (oil).

In contrast to the decrease of BC yields at vitiated conditions, the aerosol mass yields for the cable materials were similar (C08) or increased (C04). This is likely related to reduced combustion temperatures and less efficient oxidation of low volatility pyrolysis gases during vitiated combustion.

Aerosol mass and BC yields were also obtained for high heat flux ( $50 \text{ kW/m}^2$ ) and three  $\text{O}_2$  concentrations (15%, 17%, and 21%) of samples C04 and C08 (Figure 18). At a heat flux of  $50 \text{ kW/m}^2$ , the decreasing effect on BC yields is less pronounced to that obtained at a heat flux of  $30 \text{ kW/m}^2$ . The result of decreasing  $\text{O}_2$  concentrations at a heat flux of  $50 \text{ kW/m}^2$  appear to be a decrease in aerosol mass and BC yields of approximately 10-30%.

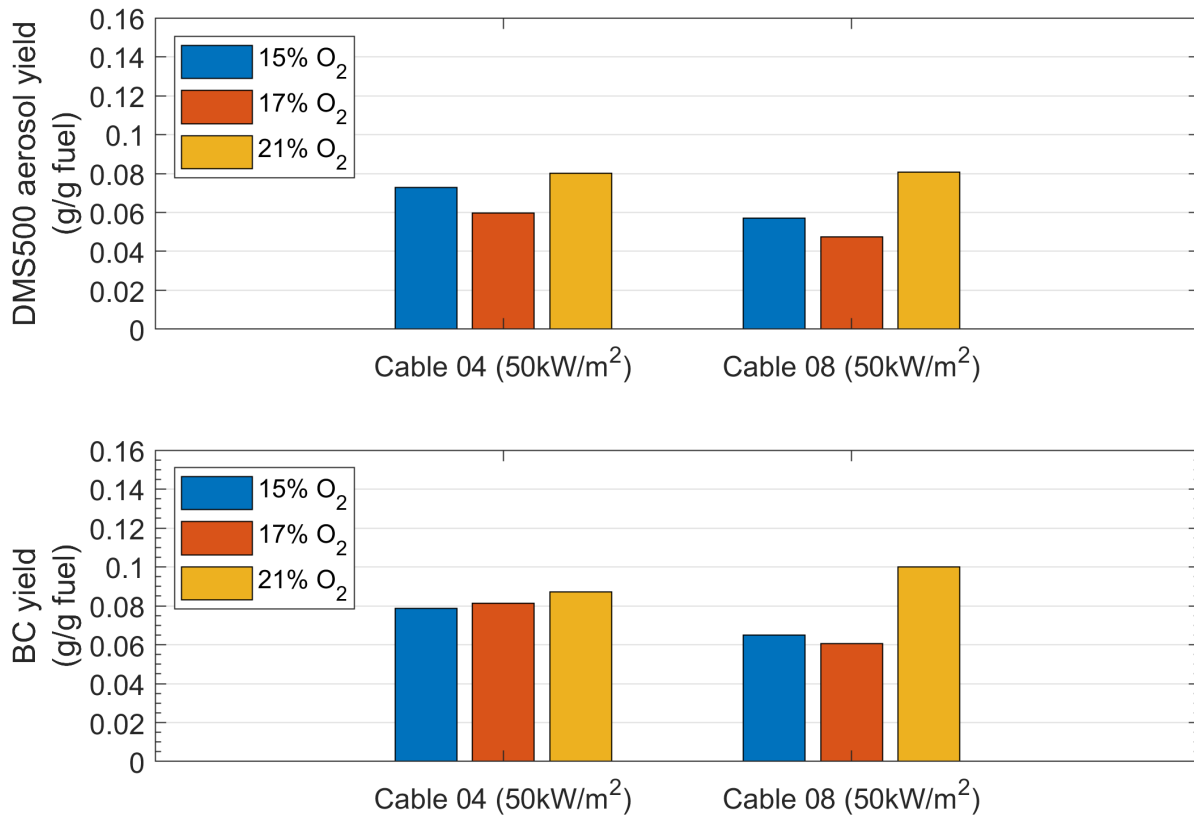


**Figure 18. Aerosol mass yields (DMS500) and BC yields for cable 04 and 08 at two levels of vitiated air (15% and 17%  $\text{O}_2$ ) and combustion at normal condition (21%  $\text{O}_2$ ) with a heat flux of  $50 \text{ kW/m}^2$ . Data refers to test numbers: 2, 53, and 56 for cable 04 (21%, 17%, 15%), and 46, 54, and 57 for cable 08 (21%, 17%, 15%).**

## 4.4 Offline analysis on particle morphology and elemental composition

Two samples were chosen for detailed off line characterization of particle morphology and elemental composition. This included an oil sample combusted at 20 kW/m<sup>2</sup> at ambient oxygen concentration and a cable sample at vitiated combustion (14% O<sub>2</sub>) at a heat flux of 50 kW/m<sup>2</sup>. These two samples were chosen as they had vastly different black carbon fractions, with the oil sample having a high BC fraction (~1.3) and the cable sample at vitiated combustion had a low BC fraction (~0.3).

### 4.4.1 Particle Imaging by Transmission Electron Microscopy

A high number of soot agglomerates were found in the oil sample with high BC fraction (figure 19). The particle shape is typical for refractory black carbon (soot) aggregates formed by diffusion-limited aggregation in flames. The primary particle size is ~ 30-50 nm (a statistical analysis is beyond the scope of this work). This is larger than for diesel exhaust where primary particle sizes are in the range 20-30 nm (Park et al. 2003). The mobility size can often be approximated by the average of the maximum aggregate length and the aggregate width. Applying this to the particles in the figure yields a size of about 300-500 nm, which is close to the mass distribution peak diameter found for this sample (300 nm). The primary particle diameter is a controlling variable for the effective density (and mass) for a given mobility diameter. The effective density increases with increasing primary particle diameter. This may be the explanation that the effective density in this study is generally higher than for diesel exhaust for a given particle size (Figure 14).

The sample in figure 20 was collected during vitiated (oxygen reduced) combustion conditions. Very few particles were found on the TEM grid (n=7). The identified particles showed a variety of shapes, therefore the particle types in the figure can not be regarded as representative. However, these results are still compatible with the online measurements that show low BC fractions. Organic particles with higher volatility are not expected to be seen in the TEM as they would evaporate either due to the low pressure or the radiation from the electron beam.

Qualitative Electron Dispersive X-ray Spectroscopy (EDX) showed that the particles were strongly dominated by carbon. No other elemental signal except the expected method-derived elements (Cu, O, Si) from the detector and grid was found. From this we can conclude that elements that can be detected with EDX ( $Z < 11$ ) were in general below the method detection limit of 0.1% of total mass. This puts an upper limit of the yields of these elements of  $< 1 \cdot 10^{-4}$  for sample T37 and  $< 5 \cdot 10^{-5}$  for sample T59.

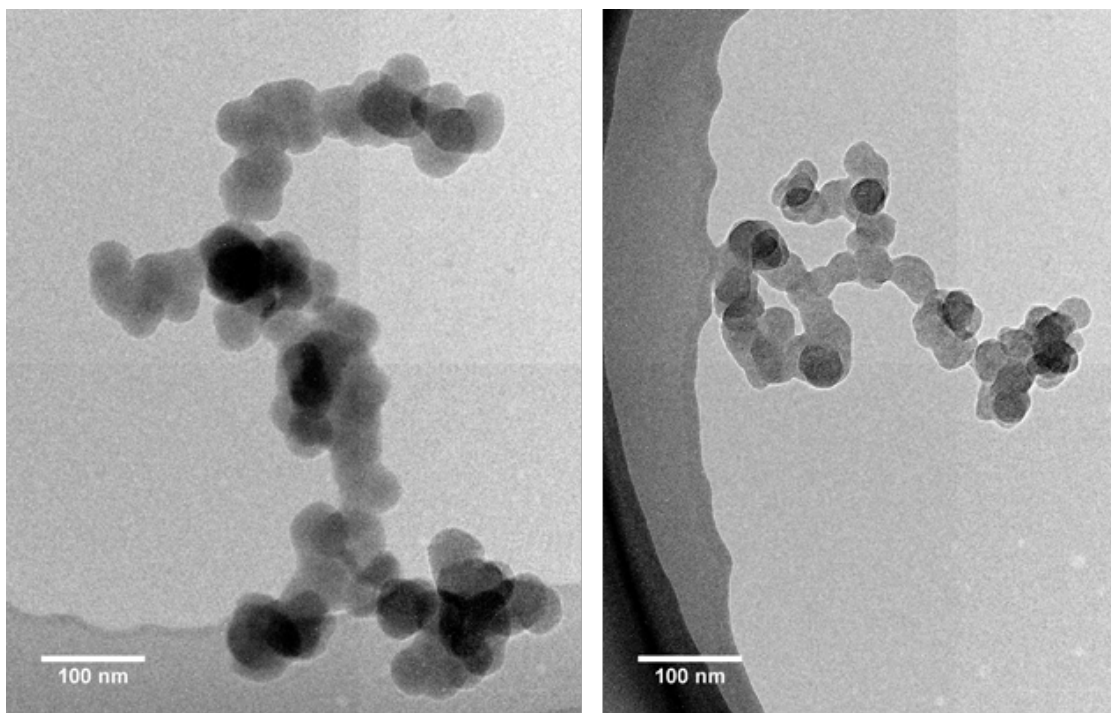


**Figure 19.** TEM images of sample T37\_O02\_20\_5mm. This is an oil sample combusted at 20 kW/m<sup>2</sup> at ambient oxygen concentration. These are representative particles chosen from a large number of analysed particles. The morphology and size is typical for soot agglomerates from combustion processes.

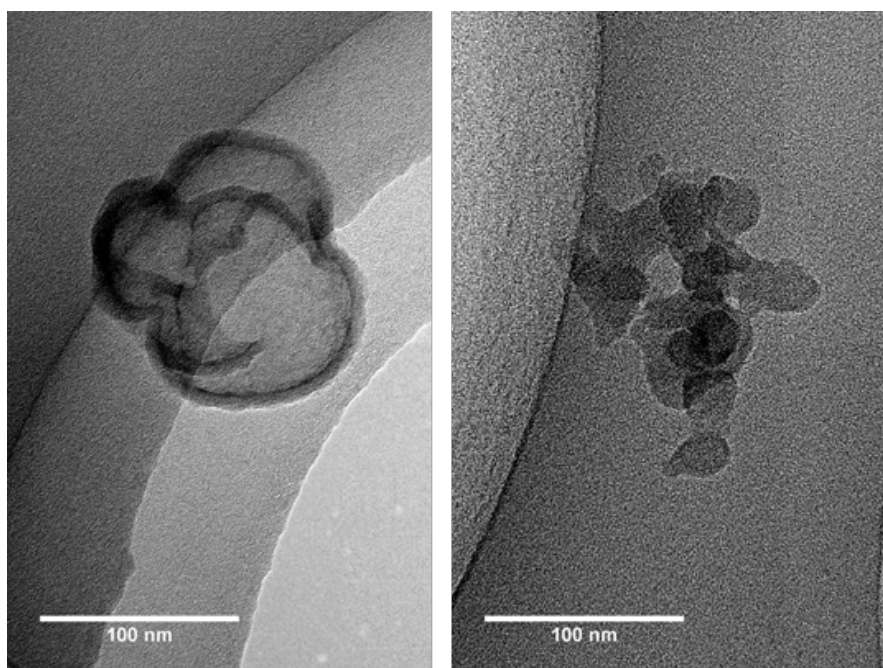


**Figure 20.** TEM images of sample T59\_C04\_30\_1L\_US\_O14. This sample is from vitiated combustion for a cable sample. Very few particles were found on these substrates (in total 7 particles), therefore it can not be said that these particles are representative.

#### 4.4.2 Elemental analysis by Inductively Coupled Plasma Mass Spectroscopy

The detected elements were low in concentration, in most cases below the detection limit of the ICP-MS method (Table 4). Both samples showed slightly higher Al and Mg concentration compared to the blank filter value. However, the differences were small, 5-20% above the blank value. Therefore these numbers should be treated with care.

**Table 4. Yields of selected elements according to the ICP-MS analysis**

Element	T37 O02 20 05MM US	T59 C04 30 IL US O14
Be	$<6 \cdot 10^{-7}$	$<2 \cdot 10^{-6}$
Na	$<6 \cdot 10^{-3}$	$<2 \cdot 10^{-2}$
Mg	$(6 \cdot 10^{-5})$	$(4 \cdot 10^{-5})$
Al	$(5 \cdot 10^{-5})$	$(4 \cdot 10^{-5})$
Si	$<3 \cdot 10^{-2}$	$<8 \cdot 10^{-2}$
P	$<3 \cdot 10^{-4}$	$<8 \cdot 10^{-4}$
S	$<3 \cdot 10^{-3}$	$<8 \cdot 10^{-3}$
Cl	$<2 \cdot 10^{-3}$	$<4 \cdot 10^{-3}$
V	$<1 \cdot 10^{-6}$	$<4 \cdot 10^{-6}$
Cd	$<6 \cdot 10^{-6}$	$<2 \cdot 10^{-6}$
Co	$<6 \cdot 10^{-6}$	$<2 \cdot 10^{-6}$
Cu	$<3 \cdot 10^{-5}$	$<8 \cdot 10^{-5}$

There are several reason for the difficulty to quantify the elemental composition in this study. The first is that the sampling was done after dilution with a relatively low flow rate. This approach is commonly working well for conventional emission sampling from sources such as diesel exhaust and biomass combustion. However, mass yields found in this study were 10-1000 times higher than for more common sources. The emissions detected here were therefore strongly dominated by carbon species due to the strong soot formation and emission. This led to the inability to detect the elements using TEM-EDX (detection limit  $\sim 1000$  ppm of collected PM mass). The PM emission factors for the two cases analysed were 50-100 mg/g<sub>fuel</sub> (mass yields 0.05-0.10). Corresponding numbers for biomass combustion are 0.1-5 mg/g<sub>fuel</sub> (mass yields 0.0001-0.005). ICP-MS is a very sensitive method for trace elements such as V, Cd and Cu. However, it is less sensitive for intermediate elements such as S, Cl, Si and Na that are of interest for FIRIA.

Emissions of light elements such as Hydrogen require additional methods for detection. The general understanding is that the Hydrogen content can be high for organic components, but that it decreases with increasing BC fraction of the emissions. For mature soot particles the H:C ratio is low, typically below 0.1 (Alfe et al. 2009). An improved estimate could also be obtained if the

carbon is fractionated into elemental and organic carbon using thermal optical analysis. Hydrogen may also be released in form of water vapour and as gas-phase hydrocarbons, neither of which were measured here.

In future studies a higher filter mass should be collected for ICP-MS analysis and it is clear that TEM-EDX is not a suitable method when the ash content is low and the soot yields are very high. In addition to elemental analysis with ICP-MS, on-line aerosol mass spectrometry may be used to determine the hydrogen and oxygen contribution. It should be mentioned that several species of interest for FIRIA may be primarily released in the gas-phase, examples are sulphur as SO<sub>2</sub>, nitrogen as NO<sub>x</sub> and chloride as HCl. These species may be transformed in the atmosphere forming oxidised products such as sulphate and nitrate that condenses on particles and thus their further transport is determined by the removal rate of particles.

To fully understand the release of potentially radioactive elements, the elemental composition of the sample (cable, oil etc) should preferentially be known beforehand. Then a complete mass balance can be done highlighting emissions in gas and particle phase, respectively as well as ash that is left in the sample after the fire.

## 4.5 Error and sensitivity analysis

### 4.5.1 DGI filter weighing

In the gravimetric impactor (DGI) analysis filter weighing is performed. The filters were weighted 2 times before and 2 times after collection. The average of the filter weight before collection is subtracted from the average of the filter weight after collection to yield the collected pm mass. In order to assess for fluctuations of the filter material (for example water uptake) itself the filters are corrected for the difference of blank filters weight on the same days. The associated filter weighing error was derived from the standard deviation of the blank filters and the 2 filter weights. The relative error from  $\pm 2$  std related to each DGI measurement is presented in Table 5.

**Table 5. DGI relative errors (assuming  $\pm 2$  std) associated with the filter weighing procedure.**

<b>Test ID</b>	T2	T19	T20	T21	T22	T27	T28	T31	T37	T38	T59	T60	T61	<b>Average relative error</b>
<b>Relative error</b>	0.07	0.26	0.08	0.04	0.25	0.26	0.19	0.17	0.06	0.88	0.64	0.23	0.14	<b>0.25</b>

### 4.5.2 Sensitivity analysis of the APM and DMS500 mass derivation

The accuracy of the APM analysis depend on several factors, including: the representativeness of the average particle mass for a given size in the 10 liters mixing volume, the precision of the chosen

electrical mobility diameter, the calibration slope of the APM, and finally the choice of electrical mobility diameters and the assumptions made for interpolating between and extrapolating outside the measured APM particle size interval.

Because the exact error related to the APM cannot be determined, a sensitivity analysis of the DMS500 mass yield derivation was instead performed. The sensitivity analysis was performed on the cone calorimeter calibration material PMMA, for which three individual tests were consecutively performed. The effective particle densities for the three tests is shown in Figure 21.

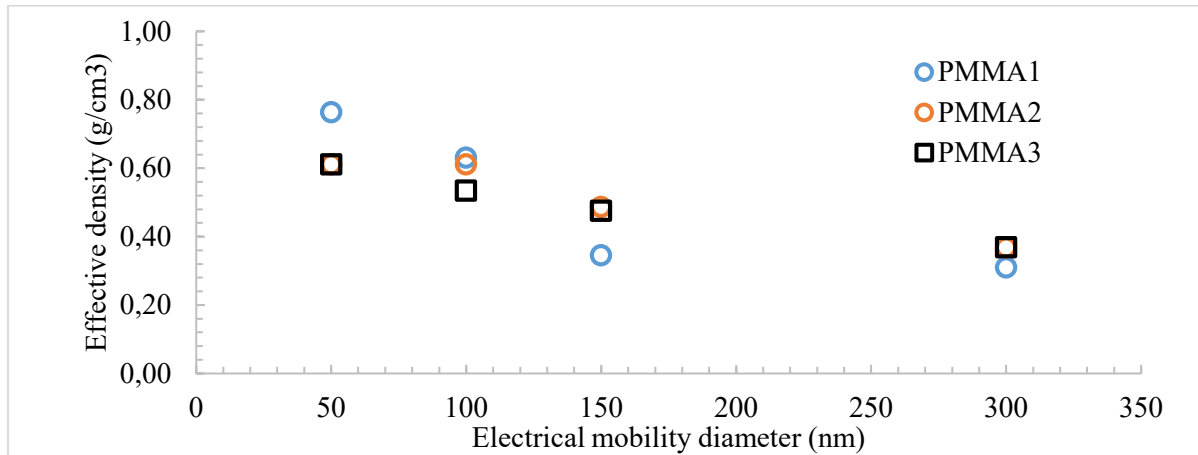


**Figure 21. Effective particle densities for three individual measurements of PMMA.**

In order to assess the sensitivity of the DMS500 mass yield derivation which relies on the DMA-APM results, the effective density distributions from the three PMMA burns in Figure 21 (PMMA1, PMMA2, PMMA3) were assigned to the first PMMA test (PMMA1). The result of the sensitivity analysis is summarized in Table 6. For the PMMA, the sensitivity of the estimated DMS500 aerosol mass yield to small fluctuations in the APM derived effective density distribution is on the order of 20%, similar to the estimated error of the DGI filter weighing procedure.

**Table 6. Sensitivity analysis of the DMS500 aerosol mass yield.**

APM data from test	APM particle sizes (nm)				Effective density (g/cm <sup>3</sup> )				Aerosol mass yield (g/g fuel)	Average aerosol mass yield, $\pm 2$ std (g/g fuel)
PMMA1					0.76	0.63	0.35	0.31	0.01067	<b>0.0122 <math>\pm 0.0026</math></b>
PMMA2	50	100	150	300	0.61	0.61	0.49	0.37	0.01297	
PMMA3					0.61	0.53	0.48	0.37	0.01285	

#### 4.5.3 Comparison of aerosol yields derived for the DGI and DMS500 instruments

For the primary analysis, aerosol mass yields were derived from simultaneous measurements with the DGI impactor and DMS500. The mass yields reported from the DGI impactor includes particle sizes up to the cut-off diameter of the pre-cyclone ( $\sim 6 \mu\text{m}$ ). However, the evaporation of semi volatile particle material may lead to an underestimation of the sampled particle mass for non-solid aerosols. The DMS500 classifies particle mass and number yields in the size range 5-1000 nm. The number yield is well defined to particle sizes  $< 1000 \text{ nm}$ . The mass yields derived for the DMS500 will underestimate the total mass yield for aerosols with significant mass fraction at particle sizes  $> 1000 \text{ nm}$ . The comparison between aerosol mass yields derived for the DGI and DMS500 measurements are shown in Figure 22. The aerosols yields derived for the two independent instruments are in good agreement but the DMS500 mass yield appear to, on average, be approximately 20% higher compared to the DGI mass yield.

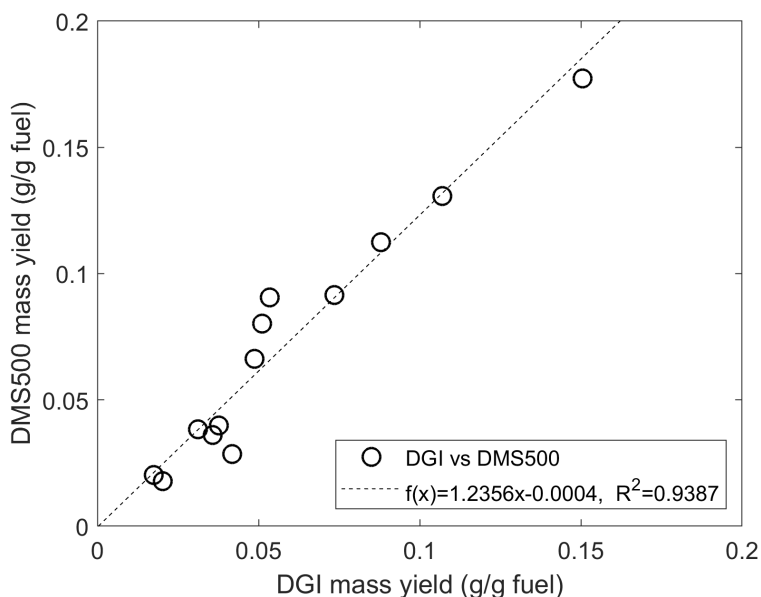


Figure 22. Comparison of aerosol mass yields derived for measurements obtained with the DGI and DMS500 respectively.



## 5 Conclusions

- Particle mass yields were in the range 0.005 to 0.23 gram per gram fuel, with higher values for electrical components and magnets, and lower values for cables and low heat fluxes.
- In most experiments the size distribution could be divided into a nucleation mode and a larger accumulation mode.
- The accumulation mode dominated during the most intense fires in each experiment. The nucleation mode dominated during lower conversion rates with no or only a small flame.
- The mass yields correlate well with the accumulation mode, while the number yield is often associated with the nucleation mode
- In most cases the particles were dominated by black carbon (BC), but during vitiated conditions and at low heat fluxes the BC fraction was often low. We hypothesize that low volatility organic matter from pyrolysis is the main additional contributor.
- Particle imaging using transmission Electron Microscopy showed typical refractory black carbon (soot) aggregates for a case with high BC fraction and very few particles of varied properties for a case with low BC fraction. We hypothesize that for the latter case, the majority of the organic particles evaporated from the TEM grids prior to measurement.
- Based on other studies it can be assessed that in addition to Carbon, Hydrogen emissions may be substantial, particularly for cases including low temperature pyrolysis. The yields of heavier elements could not be quantified, but could for most elements be constrained to low values.
- The mass mobility relationship depends on material and combustion conditions, with BC dominated emissions having lower mass per particle (effective density) for a given particle size compared to emissions with low BC fraction. The increased effective density at low BC fractions is hypothesized to be due to organic components that fill in the pores in the agglomerated soot particles.

### Future work:

- The elemental yields require further study. Suitable techniques are in addition to ICP-MS, thermal optical analysis (OC/EC) and highly time-resolved on-line aerosol mass spectrometry. The latter provides information on the chemical composition, for example H:C, O:C ratios and carcinogenic components such as polycyclic hydrocarbons that may form at elevated levels in low-temperature flames.

## 6 References

- Alfè, M., Apicella, B., Barbella, R., Rouzaud, J. N., Tregrossi, A., & Ciajolo, A. (2009). **Structure–property relationship in nanostructures of young and mature soot in premixed flames.** *Proceedings of the Combustion Institute*, 32(1), 697-704.
- Allen, M. D., & Raabe, O. G. (1985). **Slip Correction Measurements of Spherical Solid Aerosol Particles in an Improved Millikan Apparatus.** *Aerosol Science and Technology*, 4(3), 269-286. 10.1080/02786828508959055
- Drinovec, L., Močnik, G., Zotter, P., Prévôt, A. S. H., Ruckstuhl, C., Coz, E., . . . Hansen, A. D. A. (2015). **The "dual-spot" Aethalometer: an improved measurement of aerosol black carbon with real-time loading compensation.** *Atmospheric Measurement Techniques*, 8(5), 1965-1979. 10.5194/amt-8-1965-2015
- Gustafsson, M., Forsberg, B., Orru, H., Åström, S., Haben, T., & Sjöberg, K. (2014). **Quantification of population exposure to NO<sub>2</sub>, PM<sub>2.5</sub> and PM<sub>10</sub> and estimated health impacts in Sweden 2010.** IVL report.
- Hertzberg, T., Blomqvist, P., Dalene, M., & Skarping, G. (2003). **Particles and isocyanates from fires:** Sveriges provnings-och forskningsinstitut (SP).
- ICRP. (1994). **Human respiratory tract model for radiological protection. A report of a Task Group of the International Commission on Radiological Protection.** *Annals of the ICRP*, 24(21-23):21-482.
- Kulkarni, P., Baron, P. A., & Willeke, K. (2011). **Aerosol measurement: principles, techniques, and applications:** John Wiley & Sons.
- Pagels, J., Strand, M., Rissler, J., Szpila, A., Gudmundsson, A., Bohgard, M., ... & Swietlicki, E. (2003). **Characteristics of aerosol particles formed during grate combustion of moist forest residue.** *Journal of Aerosol Science*, 34(8), 1043-1059.
- Park, K., Cao, F., Kittelson, D. B., & McMurry, P. H. (2003). **Relationship between particle mass and mobility for diesel exhaust particles.** *Environmental Science & Technology*, 37(3), 577-583. DOI:10.1021/es025960v
- Park, K., Kittelson, D. B., & McMurry, P. H. (2004). **Structural properties of diesel exhaust particles measured by transmission electron microscopy (TEM): Relationships to particle mass and mobility.** *Aerosol Science and Technology*, 38(9), 881-889.
- Perovic, D. (2018). **Identification and characterization of design fires to be used in performance-based fire design of CERN facilities.** Master Thesis, Faculty of Engineering, Lund University. <http://lup.lub.lu.se/student-papers/record/8951634>.
- Reavell, K. (2002). **Fast response classification of fine aerosols with a differential mobility spectrometer.** *Proceeding 13th Annual Conference Aerosol Society*, 121-124.
- Reavell, K., Hands, T., & Collings, N. (2002). **A Fast Response Particulate Spectrometer for Combustion Aerosols.** *SAE Transactions*, 111, 1338-1344.
- Sakurai, H., Park, K., McMurry, P. H., Zarling, D. D., Kittelson, D. B., & Ziemann, P. J. (2003). **Size-dependent mixing characteristics of volatile and nonvolatile components in diesel exhaust aerosols.** *Environmental Science & Technology*, 37(24), 5487-5495.

